NASA/CR—2004-213069

Disk Crack Detection for Seeded Fault Engine Test

Huageng Luo, Hector Rodriguez, and Darren Hallman
GE Global Research, Niskayuna, New York

Dennis Corbly
GE Aircraft Engines, Cincinnati, Ohio

May 2004

The NASA STI Program Office . . . in Profile

Since its founding, NASA has been dedicated to the advancement of aeronautics and space science. The NASA Scientific and Technical Information (STI) Program Office plays a key part in helping NASA maintain this important role.

The NASA STI Program Office is operated by Langley Research Center, the Lead Center for NASA's scientific and technical information. The NASA STI Program Office provides access to the NASA STI Database, the largest collection of aeronautical and space science STI in the world. The Program Office is also NASA's institutional mechanism for disseminating the results of its research and development activities. These results are published by NASA in the NASA STI Report Series, which includes the following report types:

- TECHNICAL PUBLICATION. Reports of completed research or a major significant phase of research that present the results of NASA programs and include extensive data or theoretical analysis. Includes compilations of significant scientific and technical data and information deemed to be of continuing reference value. NASA's counterpart of peer-reviewed formal professional papers but has less stringent limitations on manuscript length and extent of graphic presentations.

- TECHNICAL MEMORANDUM. Scientific and technical findings that are preliminary or of specialized interest, e.g., quick release reports, working papers, and bibliographies that contain minimal annotation. Does not contain extensive analysis.

- CONTRACTOR REPORT. Scientific and technical findings by NASA-sponsored contractors and grantees.

- CONFERENCE PUBLICATION. Collected papers from scientific and technical conferences, symposia, seminars, or other meetings sponsored or cosponsored by NASA.

- SPECIAL PUBLICATION. Scientific, technical, or historical information from NASA programs, projects, and missions, often concerned with subjects having substantial public interest.

- TECHNICAL TRANSLATION. English-language translations of foreign scientific and technical material pertinent to NASA's mission.

Specialized services that complement the STI Program Office's diverse offerings include creating custom thesauri, building customized databases, organizing and publishing research results . . . even providing videos.

For more information about the NASA STI Program Office, see the following:

- Access the NASA STI Program Home Page at ***http://www.sti.nasa.gov***

- E-mail your question via the Internet to help@sti.nasa.gov

- Fax your question to the NASA Access Help Desk at 301–621–0134

- Telephone the NASA Access Help Desk at 301–621–0390

- Write to:
  NASA Access Help Desk
  NASA Center for AeroSpace Information
  7121 Standard Drive
  Hanover, MD 21076

NASA/CR—2004-213069

Disk Crack Detection for Seeded Fault Engine Test

Huageng Luo, Hector Rodriguez, and Darren Hallman
GE Global Research, Niskayuna, New York

Dennis Corbly
GE Aircraft Engines, Cincinnati, Ohio

Prepared under Contract NAS3–01135, Task 7

National Aeronautics and
Space Administration

Glenn Research Center

May 2004

Acknowledgments

Support of this work by the Glenn Research Center of the National Aeronautics and Space Administration under contract NAS3–Support of this work by the Glenn Research Center of the National Aeronautics and Space Administration under contract NAS3–01135 is gratefully acknowledged. The attention given by the Contracting Officer's Technical Representative, Dr. David G. Lewicki, is particularly appreciated. In addition, the authors would like to acknowledge Ms. Silvia Seng and the Naval Warfare Center, Weapons Division, Systems Vulnerability Branch, China Lake, California, for the support in the engine tests.

Table of Contents

List of Figures

Executive Summary

This report summarizes the results of the Task Order "Disk Crack Detection for Seeded Fault Engine Test" performed by General Electric Aircraft Engines (GE AE) and General Electric Global Research (GE GR) under the NASA Revolutionary Aerospace Engine Research Program. The objectives of this task are to develop and demonstrate vibration diagnostic techniques for the on-line detection of engine rotor disk cracks and other anomalies through a real engine test.

The existing detection techniques are based on a single-degree-of-freedom (SDOF) assumption. In reality, no system is completely described as a SDOF, especially if the sensors are stationary based. The GE team extended the existing the SDOF non-resonance-based algorithm into an MDOF based algorithm. In the case of one or more resonance frequencies in the speed range, a resonance-based algorithm is also proposed.

A rotor synchronous vibration based anomaly detection system is then integrated by using state-of-the-art commercial analysis equipment. The selected equipment was the B&K Pulse unit as the front-end and Signalysis PTA (Product Test Advisory) as the data management system. The proposed algorithms are implemented with MATLAB and interfaced with the database to carry out real-time health monitoring. The system requires only non-rotating vibration signals, such as accelerometers and proximity probes, and the rotor shaft 1/rev signal to conduct the health monitoring. These signals usually exist in an engine or can be easily installed, which make the GE system potentially appealing for real implementation.

Before the engine test, the integrated system was tested in the laboratory by using a small rotor with controlled mass unbalances. The laboratory tests verified the system integration and both the non-resonance and the resonance-based algorithm implementations. In cases where there is a resonance in the speed range, the resonance-based algorithm may provide better identification results.

In the engine test, the GE system concluded that after two weeks of cycling, the seeded fan disk flaw did not propagate to a large enough size to be detected by changes in the synchronous vibration. The unbalance induced by mass shifting during the start up and coast down was still the dominant response in the synchronous vibration. The continuation of the test in the future is recommended to generate more meaningful response data. An experimental modal test and analysis of the engine case is also recommended so that the resonant-vibration based identification method may be applied.

1. Background

1.1 Mass unbalance in rotors

The physics of the mass unbalance induced vibration response in rotors can be explained using a simplified shaft-disk assembly. Figure 1-1 shows a one degree-of-freedom Jeffcott rotor in which the shaft-disk assembly is modeled by a spring-mass system restricted to vibrate along the vertical y-axis. In this model, the disk is represented by its mass M and the stiffness of the shaft is represented by k_s. This simplified representation of the rotor is typically used to model the response of single-disk rotor

assemblies under relatively rigid bearings (e.g., ball bearings) at relatively low speeds (i.e., near or below the first bending critical speed). The amplitude of the displacement response *Y* at the center of the disk due to mass unbalance is given as[1]

$$Y = \frac{u_m \Omega^2}{M\sqrt{\left(1-\Omega^2\right)^2 + \left(2\xi\Omega\right)^2}} \tag{1-1}$$

where $u_m = me$ is the unbalance due to a finite mass *m* at a radius of rotation *e*, $\Omega = \omega / \omega_{cr}$ is the ratio of the shaft speed ω to the critical speed $\omega_{cr} = \sqrt{k_s / M}$, and ξ is the damping ratio.

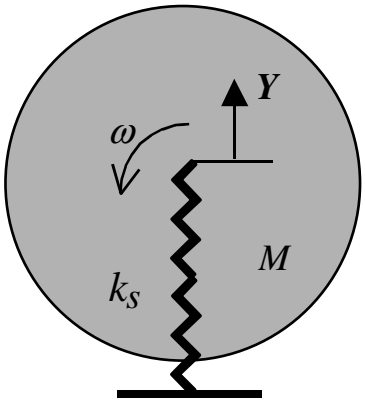

Figure 1-1.—Jeffcott Model of Rotor Assembly.

Equation (1-1) shows that at speeds below the critical speed (i.e., $\Omega < 1.0$), the vibration response due to mass unbalance is proportional to ω^2.

1.2 Crack Induced Unbalance

Cracks in rotor disks have been identified to cause a distinct behavior in the vibration response of rotor assemblies[6,7]. Radial-axial cracks induce a unique vibration response as they open due to tensile hoop stresses caused by centrifugal loading. The crack, which opens as a function of rotor speed squared, forces a redistribution of the disk mass. This redistribution results in an additional unbalance that is also proportional to the square of the speed, and hence the resulting crack-induced unbalance force is proportional to the fourth power of the speed. This unique unbalance force characteristic contrasts with the force due to standard mass unbalance, which is related to the square value of the speed.

In the case of a radial-axial crack with length *a* in a disk rotating at speed ω, the induced unbalanced can be expressed as

$$u_c(a,\omega) = m_c(a,\omega)e_c\,, \tag{1-2}$$

where the effective change in mass distribution due to the crack opening $m_c(a,\omega)$ is a function of the crack size and speed, and e_c is the effective radius of rotation of $m_c(a,\omega)$. The hoop stress in a rotating disk is a function of the square of the rotating speed ω. Therefore, the effective change in mass distribution due to the crack opening is also a function of the square of the rotating speed. The response of a Jeffcott type rotor with a radial-axial crack can be obtained after substituting $u_c(a,\omega)$ for u_m in eq. (1-1). Due to the dependence of $u_c(a,\omega)$ on ω^2, the resulting displacement response in the low-speed regime (i.e., below the critical speed) will be proportional to the fourth power of the speed.

An approximate expression for eq. (1-2) can be obtained if the effective change in mass distribution due to the crack opening is represented as a "removed" mass while e_c is the radial distance to the crack tip as shown in Figure 1-2. In the case of a radial-axial crack, the "removed" mass is proportional to the opening of the crack δ as a function of speed. The opening of a small crack in a large-diameter disk can be approximated using the analogy of an edge crack in a plate strip, for which a closed-form solution exists. The opening of the crack due to tensile hoop stress level in the neighborhood of the crack is given as[2]

$$\delta = \frac{4\sigma_h a}{E} V\left(\frac{a}{D}\right), \tag{1-3}$$

where the empirical function V(a/D) is given as[2]

$$V\left(\frac{a}{D}\right) = \frac{1.46 + 3.42 \times \left(1 - \cos\left(\frac{\pi a}{2D}\right)\right)}{\left(\cos\left(\frac{\pi a}{2D}\right)\right)^2}, \tag{1-4}$$

where the disk diameter is used instead of the plate's width as considered in the reference. As can be noticed in Eq. (1-4), $V(a/D)$ approaches the constant value of 1.46 for small ratios of a/D.

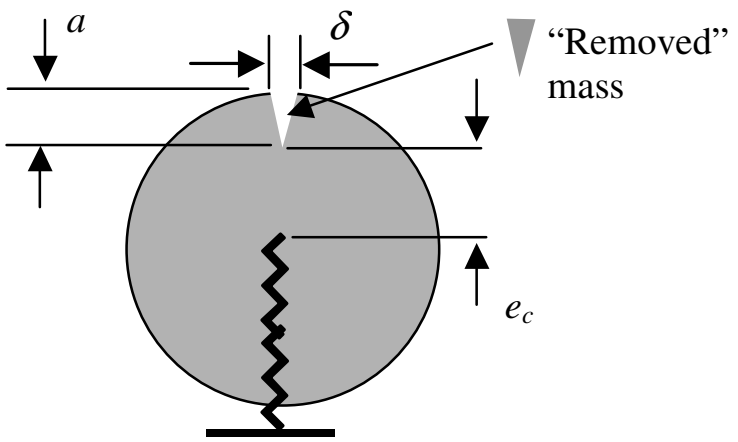

Figure 1-2.— Jeffcott Rotor Showing "Removed" Mass Concept.

The hoop stress in a constant thickness disk at a distance ec is given as[3]

$$\sigma_h = \frac{\rho D^2 \omega^2 (3+\mu)}{32g}\left(1 - \frac{(1+3\mu)}{3+\mu} \times \left(\frac{2e_c}{D}\right)^2\right), \tag{1-5}$$

where g is the gravity constant. Finally, the "removed" mass can be approximated as

$$m_c = \frac{\delta a t \rho}{2g}. \tag{1-6}$$

Therefore, the crack-induced unbalance is given as

$$u_c = K\rho^2 a^2 t D^2 \omega^2 e_c, \tag{1-7}$$

where

$$K = \frac{(3+\mu)}{16g^2 E}\left(1 - \frac{(1+3\mu)}{3+\mu} \times \left(\frac{2e_c}{D}\right)^2\right) V\left(\frac{a}{D}\right). \tag{1-8}$$

In the case of values of a/D less than 0.05, Eq. (1-8) becomes $K \sim 0.5/E$.

Equation (1-7) clearly establishes the dependence of the crack-induced unbalance on the physical parameters of the disk and the rotational speed. As shown in the equation, the crack-induced unbalance is proportional to the second power of the speed, the weight density, the crack length, and the disk diameter, respectively. In addition, for the case of relatively small cracks, e_c approximates $D/2$ introducing a

stronger dependence of the unbalance to the disk diameter. Refer to references [4,5] for more physics based crack detection and analysis.

2. New Approaches

2.1 Introduction

It has been well established that the mass-induced synchronous vibration is proportional to the square of the rotational speed, i.e. ω^2, in the region where $\omega << \omega_0$, where ω_0 is the first resonant frequency of the machinery system. The radial-axial cracks in the rotating disk or shaft can cause a synchronous vibration that is proportional to ω^4, under the same assumption of $\omega << \omega_0$. Several groups have developed detection systems based on these assumptions[6,7]. Unfortunately, in reality, there are several major difficulties in implementing the traditional algorithms:

1. It is difficult to satisfy the $\omega << \omega_0$ condition without significantly reducing the signal to noise ratio, because the first natural frequency in many rotational machinery systems is very low. Especially in soft-mounted rotor systems, where the first natural frequency can be so low that it prevents such monitoring systems from getting meaningful results.
2. It is difficult to simplify real rotor machinery into a single degree of freedom (SDOF) system. On top of the bearing DOFs, the vibration sensors are usually mounted on the bearing case or engine case, so that additional structural resonances, besides rotor-shaft resonances, may be picked up, thus destroying the simple polynomial relationship.
3. The operational frequency range is not always below first resonance frequency of the rotor machinery system.

In this research, the following two new algorithms are developed for multi-degree of freedom (MDOF) rotor machinery mass unbalance and crack detection:

1. A non-resonant synchronous vibration based detection algorithm for any operational speed region between two consecutive natural frequencies of a machinery system.
2. A resonant synchronous vibration based detection algorithm for any operational speed that crosses one or more system natural frequencies.

2.2 Non-Resonant Synchronous Vibration Based Approach

In the simplest possible model for rotor vibration analysis, the system is described by a spring-mass-damper single-degree-of-freedom (SDOF) system as shown in Figure 2-1. With this model, the system has to be either a rigid rotor and disk with a flexible bearing, or a flexible mass-less rotor shaft with a rigid bearing and single rigid disk. Under these assumptions, the frequency domain vibration due to mass unbalance can be expressed as

$$Y(j\omega) = \frac{U_m \omega^2}{m\left(\omega_0^2 - \omega^2 + 2j\xi_0\omega_0\omega\right)}, \tag{2-1}$$

where

Y is the Laplace transform of y(t). $Y(j\omega) = L\left[y(t)\right]\Big|_{s=j\omega}$

j is the complex symbol, $j = \sqrt{-1}$

m is the equivalent mass of the system;

U_m is the mass unbalance in frequency domain. Its amplitude, $|U_m|=u_m$, and the phase angle, θ, as shown in Figure 2-1.

$\omega_0 = \sqrt{\frac{k}{m}}$ is the natural frequency of the system;

$\xi_0 = \frac{c}{2\omega_0 m}$ is the damping ratio of the system.

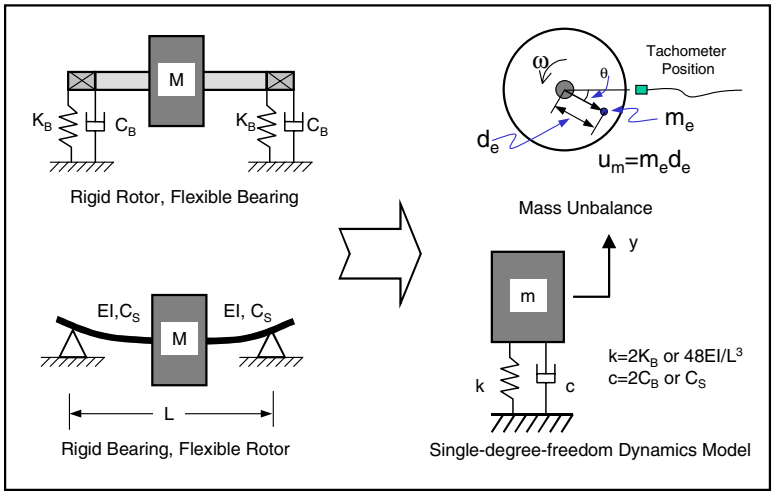

Figure 2-1.—SDOF Rotor Dynamics Modeling.

The presence of certain cracks in the rotor disk introduce similar vibration to that caused by a mass unbalance, i.e.,

$$Y(j\omega) = \frac{U_C \omega^2}{m\left(\omega_0^2 - \omega^2 + 2j\xi_0\omega_0\omega\right)} \tag{2-2}$$

where U_C is the crack induced unbalance. It is a complex variable in frequency domain. As indicated in Section 1.2, U_C is a function of rotational speed, crack length, and rotor disk geometry, more precisely,

$$U_C = K_C\omega^2 = K_C(crack, disk)\omega^2 \tag{2-3}$$

Thus, with presence of mass unbalance and a crack, the SDOF rotor possesses a vibration response format as

$$Y(j\omega) = \frac{U_m\omega^2}{m\left(\omega_0^2 - \omega^2 + 2j\xi_0\omega_0\omega\right)} + \frac{K_C\omega^4}{m\left(\omega_0^2 - \omega^2 + 2j\xi_0\omega_0\omega\right)} \tag{2-4}$$

In the region where $\omega << \omega_0$, equation (2-4) can be simplified as

$$Y(j\omega) = \frac{U_m\omega^2}{m\omega_0^2} + \frac{K_C\omega^4}{m\omega_0^2} = C_2\omega^2 + C_3\omega^4 \tag{2-5}$$

where

$$C_2 = \frac{U_m}{m\omega_0^2}; \qquad C_3 = \frac{K_C}{m\omega_0^2} \tag{2-6}$$

are the unbalance and system parameter related complex constants.

Real rotational meachinery can rarely be modeled as an SDOF system. It is usually a distributed system with infinitely many DOFs and usually a low first resonance frequency. In such cases, the system response has to be modified into a multi-degree-of-freedom (MDOF) system, assuming the system has distict natural frequencies for simplicity, as

$$\begin{aligned} Y(j\omega) = &\sum_{i=1}^{\infty} \frac{U_{mi}\omega^2}{m_i\left(\omega_i^2 - \omega^2 + 2j\xi_i\omega_i\omega\right)} \\ &+ \sum_{i=1}^{\infty} \frac{K_{Ci}\omega^4}{m_i\left(\omega_i^2 - \omega^2 + 2j\xi_i\omega_i\omega\right)} \end{aligned} \tag{2-7}$$

where U_{mi} is the i^{th} modal response due to mass unbalance coefficient; K_{Ci} is the i^{th} modal response coefficient due to crack unbalace; m_i is the i^{th} modal mass; ξ_i is the i^{th} modal damping ratio; and

$$\omega_1 < \omega_2 < \cdots < \omega_{k-1} < \omega_k < \cdots \tag{2-8}$$

are natural frequencies of the machinery system.

In the frequency region of $\omega_{k-1} < \omega < \omega_k$, the variables $\frac{\omega_i}{\omega}, i = 1,2,\cdots,k-1$ and $\frac{\omega}{\omega_i}, i = k, k+1, \cdots$ are small, thus equation (2-7) can be approximated as

$$
\begin{aligned}
Y(j\omega) = &\sum_{i=1}^{k-1} \frac{U_{mi}\omega^2}{m_i} \frac{1}{\omega^2\left[\left(\frac{\omega_i}{\omega}\right)^2 - 1 + 2j\xi_i\left(\frac{\omega_i}{\omega}\right)\right]} \\
&+ \sum_{i=k}^{\infty} \frac{U_{mi}\omega^2}{m_i} \frac{1}{\omega_i^2\left[1 - \left(\frac{\omega}{\omega_i}\right)^2 + 2j\xi_i\left(\frac{\omega}{\omega_i}\right)\right]} \\
&+ \sum_{i=1}^{k-1} \frac{K_{Ci}\omega^4}{m_i} \frac{1}{\omega^2\left[\left(\frac{\omega_i}{\omega}\right)^2 - 1 + 2j\xi_i\left(\frac{\omega_i}{\omega}\right)\right]} \\
&+ \sum_{i=k}^{\infty} \frac{K_{Ci}\omega^4}{m_i} \frac{1}{\omega_i^2\left[1 - \left(\frac{\omega}{\omega_i}\right)^2 + 2j\xi_i\left(\frac{\omega}{\omega_i}\right)\right]}
\end{aligned}
\tag{2-9}
$$

Using the Taylor series expansion and retaining up to 2nd order terms, we have

$$
\begin{aligned}
Y(j\omega) = &\sum_{i=1}^{k-1} -\frac{U_{mi}}{m_i}\left[1 + 2j\xi_i\left(\frac{\omega_i}{\omega}\right) + \left(1 - 4\xi_i^2\right)\left(\frac{\omega_i}{\omega}\right)^2 + O\left(\frac{\omega_i}{\omega}\right)^3\right] \\
&+ \sum_{i=k}^{\infty} \frac{U_{mi}}{m_i}\left[\left(\frac{\omega}{\omega_i}\right)^2 + O\left(\frac{\omega}{\omega_i}\right)^3\right] \\
&+ \sum_{i=1}^{k-1} -\frac{K_{Ci}\omega^2}{m_i}\left[1 + 2j\xi_i\left(\frac{\omega_i}{\omega}\right) + \left(1 - 4\xi_i^2\right)\left(\frac{\omega_i}{\omega}\right)^2 + O\left(\frac{\omega_i}{\omega}\right)^3\right] \\
&+ \sum_{i=k}^{\infty} \frac{K_{Ci}\omega^2}{m_i}\left[\left(\frac{\omega}{\omega_i}\right)^2 + O\left(\frac{\omega}{\omega_i}\right)^3\right]
\end{aligned}
\tag{2-10}
$$

2.2.1 Zero-order Approximation

By omitting the 1st order and higher order small terms in (2-10), we get a zero-order approximation as

$$
Y(j\omega) = -\sum_{i=1}^{k-1} \frac{U_{mi}}{m_i} - \sum_{i=1}^{k-1} \frac{K_{Ci}\omega^2}{m_i} \tag{2-11}
$$

In the case of k=2, which means the operation speed range is between the 1st and 2nd resonant frequencies, equation (2-11) is further simplified as

$$
Y(j\omega) = -\frac{U_{m1}}{m_1} - \frac{K_{C1}\omega^2}{m_1} \tag{2-12}
$$

Keep in mind that in equation (2-12), U_{m1} and K_{C1} are complex variables. Their amplitudes reflect the unbalance amounts while the phases reflect the circumferential locations. The negative signs in equation (2-12) reflect the 180° phase shift after the resonance.

2.2.2 First-order Approximation

By omitting the 2nd and higher order small terms in (2-10), we get a first-order approximation as

$$Y(j\omega) = \sum_{i=1}^{k-1} -\frac{U_{mi}}{m_i}\left[1 + 2j\xi_i\left(\frac{\omega_i}{\omega}\right)\right] + \sum_{i=1}^{k-1} -\frac{K_{Ci}\omega^2}{m_i}\left[1 + 2j\xi_i\left(\frac{\omega_i}{\omega}\right)\right] \tag{2-13}$$

In a lightly damped case, ξ_i is small, thus eq. (2-13) can be reduced to (2-11), the zero-order case. Therefore, in a lightly damped case, zero-order and 1st-order approximations are the same.

2.2.3 Higher-order Approximation

Any higher-order approximation can be derived from equation (2.9). For example, by omitting the 3rd and higher order terms in equation (2-10), we have

$$\begin{aligned} Y(j\omega) = &\sum_{i=1}^{k-1} -\frac{U_{mi}}{m_i}\left[1 + 2j\xi_i\left(\frac{\omega_i}{\omega}\right) + \left(1 - 4\xi_i^2\right)\left(\frac{\omega_i}{\omega}\right)^2\right] + \sum_{i=k}^{\infty} \frac{U_{mi}}{m_i}\left(\frac{\omega}{\omega_i}\right)^2 \\ &+ \sum_{i=1}^{k-1} -\frac{K_{Ci}\omega^2}{m_i}\left[1 + 2j\xi_i\left(\frac{\omega_i}{\omega}\right) + \left(1 - 4\xi_i^2\right)\left(\frac{\omega_i}{\omega}\right)^2\right] + \sum_{i=k}^{\infty} \frac{K_{Ci}\omega^2}{m_i}\left(\frac{\omega}{\omega_i}\right)^2 \end{aligned} \tag{2-14}$$

In a lightly damped case, ξ_i is small, thus equation (2-14) can be further reduced to

$$\begin{aligned} Y(j\omega) = &\sum_{i=1}^{k-1} -\frac{U_{mi}}{m_i}\left[1 + 2j\xi_i\left(\frac{\omega_i}{\omega}\right) + \left(\frac{\omega_i}{\omega}\right)^2\right] + \sum_{i=k}^{\infty} \frac{U_{mi}}{m_i}\left(\frac{\omega}{\omega_i}\right)^2 \\ &+ \sum_{i=1}^{k-1} -\frac{K_{Ci}\omega^2}{m_i}\left[1 + 2j\xi_i\left(\frac{\omega_i}{\omega}\right) + \left(\frac{\omega_i}{\omega}\right)^2\right] + \sum_{i=k}^{\infty} \frac{K_{Ci}\omega^2}{m_i}\left(\frac{\omega}{\omega_i}\right)^2 \end{aligned} \tag{2-15}$$

Rearranging equation (2-15), we have

$$\begin{aligned} Y(j\omega) = &-\frac{1}{\omega^2}\sum_{i=1}^{k-1}\frac{U_{mi}}{m_i}\omega_i^2 - \frac{1}{\omega}\sum_{i=1}^{k-1}\frac{U_{mi}}{m_i}2j\xi_i\omega_i \\ &-\left(\sum_{i=1}^{k-1}\frac{U_{mi}}{m_i} + \sum_{i=1}^{k-1}\frac{K_{Ci}}{m_i}\omega_i^2\right) - \omega\sum_{i=1}^{k-1}\frac{K_{Ci}}{m_i}2j\xi_i\omega_i \\ &+\omega^2\left(\sum_{i=k}^{\infty}\frac{U_{mi}}{m_i\omega_i^2} - \sum_{i=1}^{k-1}\frac{K_{Ci}}{m_i}\right) + \omega^4\sum_{i=k}^{\infty}\frac{K_{Ci}}{m_i\omega_i^2} \\ &= \frac{C_{-2}}{\omega^2} + \frac{C_{-1}}{\omega} + C_0 + C_1\omega + C_2\omega^2 + C_4\omega^4 \end{aligned} \tag{2-16}$$

where

$$
\begin{aligned}
C_{-2} &= -\sum_{i=1}^{k-1} \frac{U_{mi}}{m_i} \omega_i^2 \\
C_{-1} &= -\sum_{i=1}^{k-1} \frac{U_{mi}}{m_i} 2j\xi_i\omega_i \\
C_0 &= -\left(\sum_{i=1}^{k-1} \frac{U_{mi}}{m_i} + \sum_{i=1}^{k-1} \frac{K_{Ci}}{m_i} \omega_i^2 \right) \\
C_1 &= -\sum_{i=1}^{k-1} \frac{K_{Ci}}{m_i} 2j\xi_i\omega_i \\
C_2 &= \left(\sum_{i=k}^{\infty} \frac{U_{mi}}{m_i\omega_i^2} - \sum_{i=1}^{k-1} \frac{K_{Ci}}{m_i} \right) \\
C_4 &= \sum_{i=k}^{\infty} \frac{K_{Ci}}{m_i\omega_i^2}
\end{aligned}
\tag{2-17}
$$

are the unbalance and system parameter related complex constants.

2.3 Resonance Synchronous Vibration Based Approach

The algorithm in Section 2.2 is suitable for the non-resonant case, i.e. the vibration sensor does not pick up any system resonance in the rotor machinery operational speed range. If the sensor response includes one or more resonant frequencies in the rotor machinery operational speed range, an approach different from that proposed in section 2.2 is required.

With resonant frequencies, the displacement sensor response in the frequency domain is the same as in equation (2-7)

$$
\begin{aligned}
Y(j\omega) = &\sum_{i=1}^{\infty} \frac{U_{mi}\omega^2}{m_i\left(\omega_i^2 - \omega^2 + 2j\xi_i\omega_i\omega\right)} \\
&+ \sum_{i=1}^{\infty} \frac{K_{Ci}\omega^4}{m_i\left(\omega_i^2 - \omega^2 + 2j\xi_i\omega_i\omega\right)}
\end{aligned}
\tag{2-18}
$$

only in this case, the operational frequency range $\omega=[\omega_{01}, \omega_{02}]$, and

$$
\begin{cases}
\omega_{01} < \omega < \omega_{02} \\
\omega_k < \omega_{01} < \omega_{k+1} \text{ and } \omega_{k+l} < \omega_{02} < \omega_{k+l+1} \\
k \geq 1 \text{ or } \omega_k = 0 \\
l \geq 1
\end{cases}
\tag{2-19}
$$

Again, it is assumed here that all the resonant frequencies are well separated and that the modal cross coupling from modes outside the operational range are minimal. Thus equation (2-18) can be expressed into a finite summation as

$$Y(j\omega) = \sum_{i=k}^{l} \frac{U_{mi}\omega^2}{m_i\left(\omega_i^2 - \omega^2 + 2j\xi_i\omega_i\omega\right)} + \sum_{i=k}^{l} \frac{K_{Ci}\omega^4}{m_i\left(\omega_i^2 - \omega^2 + 2j\xi_i\omega_i\omega\right)} \tag{2-20}$$

For a given response curve, ω_i and ξ_i , i=k, k+1, …, l, can be approximated by identifying the peak location and by the half power method, respectively. Once the initial guess of ω_i and ξ_i are obtained, an iterative method can be implemented to improve the accuracy and to solve for modal excitations or U_{mi}, and K_{Ci}.

In real situations, we are usually interested in the relative change of modal excitations, thus a baseline is established first. The difference between the real-time data acquisition and baseline are used to extract the modal excitations.

3 System Integration

3.1 Introduction

In the accelerated tests performed here, a cycle consists of speed-up, dwell, and coast-down segments simulating aircraft taking-off, cruise, and landing. This process is actually taking place in a very short time. For example, the speed-up process can be as short as 15 seconds. It is very important to have a system that can handle data acquisition, processing, and management in such a short time. Additionally, the signal from such tests is usually noisy, thus it is also critical to have a processing technique to improve the signal to noise ratio.

After a careful market search, the Pulse system by B&K was selected as the hardware platform, the Production Test Advisor (PTA) by Signalysis, Inc. was selected as the database management system, and a MATLAB based post-processing system was developed in-house and integrated into the system for real-time health monitoring.

A brief system diagram is shown in Figure 3-1.

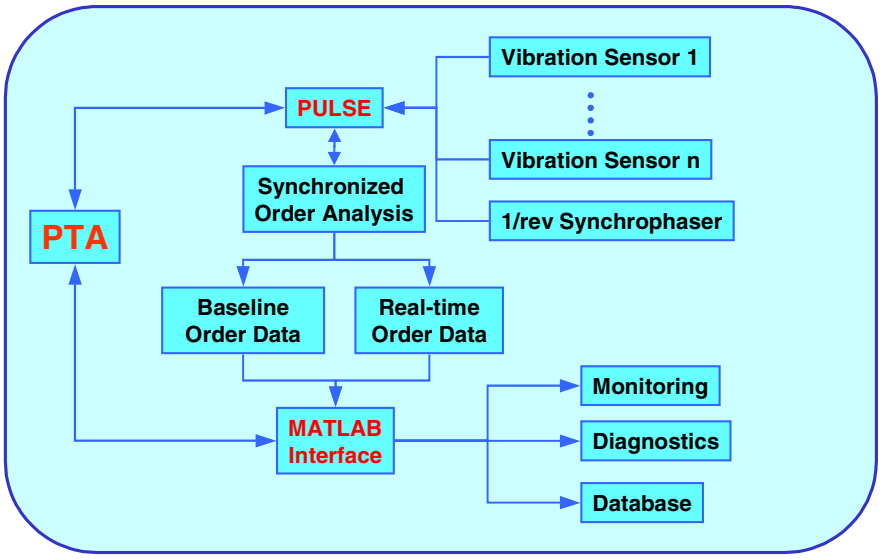

Figure 3-1.—System Diagram.

3.1 Hardware Platform

3.1.1 Sensors

Any vibration sensors, such as accelerometers, velocity sensors, or displacement probes, can be used to pick up vibration signals for the system. Appropriate signal conditioners should be supplied for the sensors used. A once per revolution (1/rev) signal from the rotating shaft is also needed for order analysis and extraction

3.1.2 Data acquisition and preprocessing

The B&K Pulse system was used as data acquisition and signal processing system. The Pulse system is a Real-time Multi-analysis platform for vibration and sound analyses.

The Order Analyzer of the Pulse system is activated for our integrations. In order to improve the signal-to-noise ratio, a synchronous averaging technique is also employed. A typical screen capture of the system is shown in Figure 3-2.

The 1st order synchronous vibration is the main focus in the system. This signal is monitored and processed real time.

The RPM Monitor window is arranged to monitor the instantaneous rotor speed.

The Status window reports the data acquisition progress.

The Run-up Waterfall window presents the overall vibration frequency (order) distribution during the speed-up. The corresponding coast-down information can also be configured as required.

The Key-phasor Monitor displays the time history of the 1/rev signal. The data acquisition trigger level can be adjusted according to the key-phasor signal.

The Overflow Monitor is used to maximize the data acquisition dynamic range while avoid the sensor signal overflow.

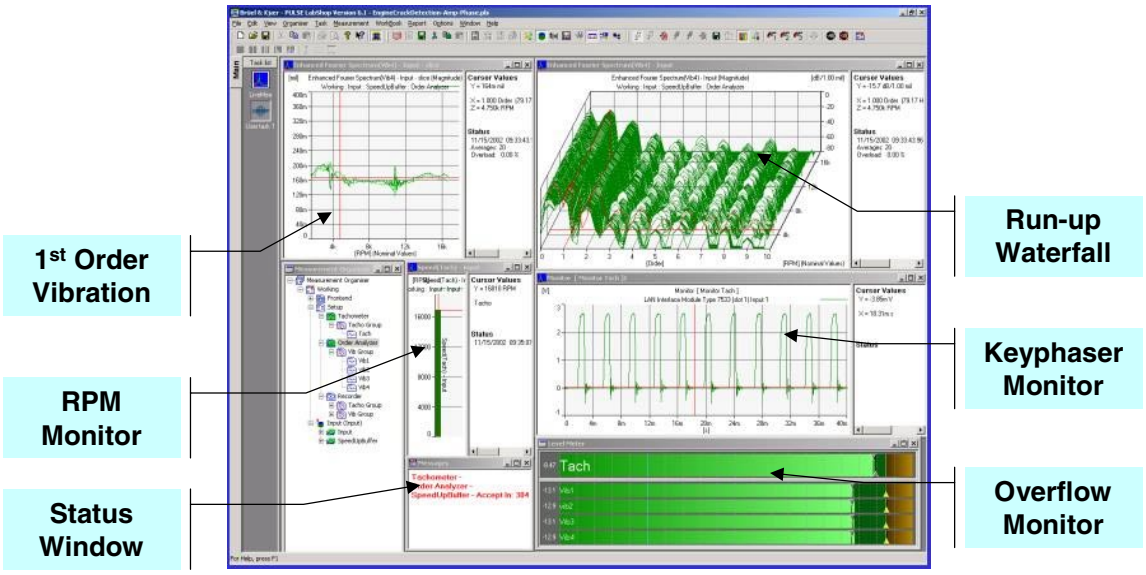

Figure 3-2.—B&K Pulse System.

3.2 Database Management

Data management for the system is carried out by the PTA (Product Test Adviser). PTA is a special version of SigQC developed by Signalysis Inc. SigQC was originally designed for manufacturer quality assurance. It is a production line test that responds to the demand among manufacturers to automate a process for accepting or rejecting units on the assembly line based on measured noise and vibration data. SigQC provides basic statistics, criteria, strategies and pass/fail methods.

The major functions of the PTA include Database Management (Database tree) and Production Line Interface (traffic control). A screen capture of the PTA is shown in Figure 3-3.

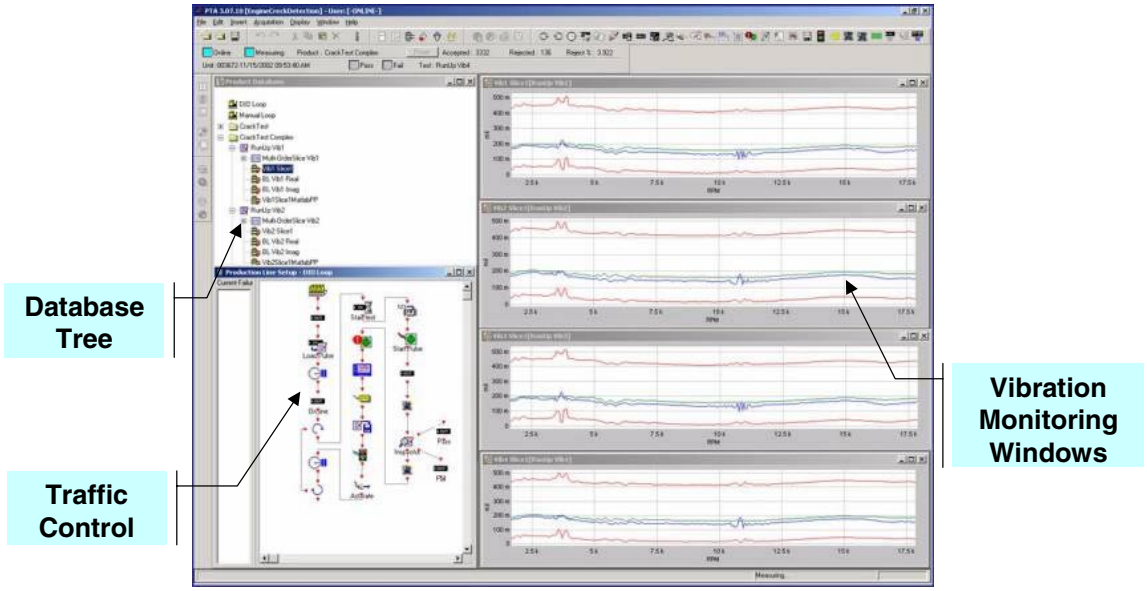

Figure 3-3.—PTA System.

3.2.1 Database Tree

The PTA data repository is integrated with the RAIMA Velocis (TM) Data Server and optimized for speed and data integrity. All database files are kept in a single folder, allowing for simple archiving of the database. Archiving the database, coupled with the database depth management capabilities, provides an easy and foolproof means of maintaining a library of all data for all parts without jeopardizing down time.

3.2.2 Traffic Control

The PTA interfaces to Programmable Logic Controllers (PLC) through Digital I/O Communications. The system is configured through the Digital I/O configuration panel. It is achieved by a simple point-and-click on the input or output and by defining the meaning of a high or low level. I/O bits can be grouped to make up a binary value (this is useful when defining model numbers or failure modes). The Digital I/O setup is used in the production line sequence for controlling the selection of model number, start/stop acquisition, pass/fail, output of failure mode, etc.

3.3 Interface and post-processing

The PTA provides basic statistics, criteria, strategies and pass/fail methods, but it is very difficult, if not infeasible, to use these basic functions to construct a diagnostic algorithm for crack detection. MATLAB codes for mass and crack unbalance detection functions were developed according to equation (2-11) for non-resonant synchronous vibration and (2-20) for resonant synchronous vibration. The codes are incorporated into the crack detection system and utilize the interface between PTA and MATLAB.

4 Small Rotor Test

To verify the crack detection system integration and algorithms, a Bently Nevada RK 4 rotor kit was used as test bench.

4.1 Setup

The test rig diagram and instrument setup are shown in Figure 4-1 and Figure 4-2, respectively. A single rotor disk with two bearings was used. The rotor disk has a weight of 810g and balance slots at radius of 30.5 mm and 22.5^{o} resolution in circumference. See Figure 4-3. The rotor shaft has a diameter of 10 mm and bearing span is 400 mm with additional 200 mm overhang. With such setup, the fundamental frequency of the system is at 2000 rpm. Modal test indicates that the second bending resonance is at about 10,000 rpm.

Proximity probes were used as the signal pick up. Sensor #1 (vib1) is in the vertical direction, while sensor #2 (vib2) is in the horizontal direction. The typical synchronous responses of the system are shown in Figure 4-4 and Figure 4-5, respectively.

Nylon set screws were used as an unbalance weight to improve the unbalance resolution. As a result, the smallest unbalance unit is 3.416 g-mm. The disk 0^{o} position was aligned with the center of the notch on the rotor shaft. A mechanical 1/rev signal (shaft notch detected by proximity probe) was used as the trigger. The rising edge of the signal was used in the trigging, which turned out to be the trailing edge of the shaft notch. Later a laser calibration indicated that the actual triggering point corresponds to approximately the 30^{o} rotor disk circumferential position.

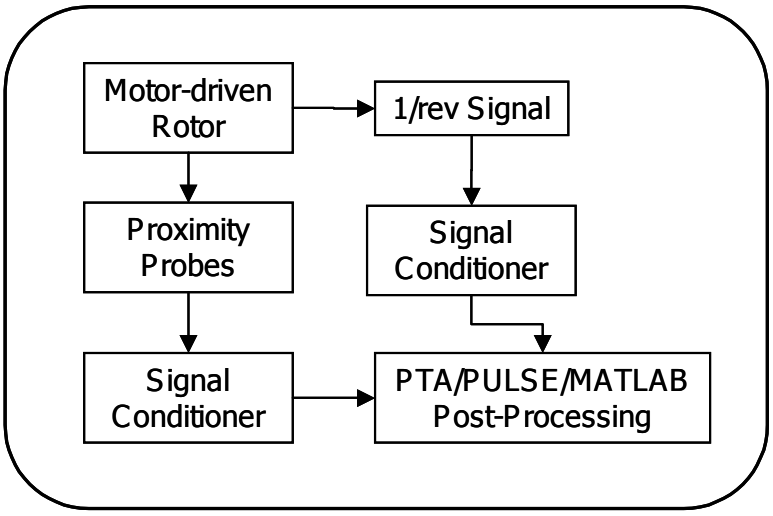

Figure 4-1.—Small Rotor Rig Test Diagram.

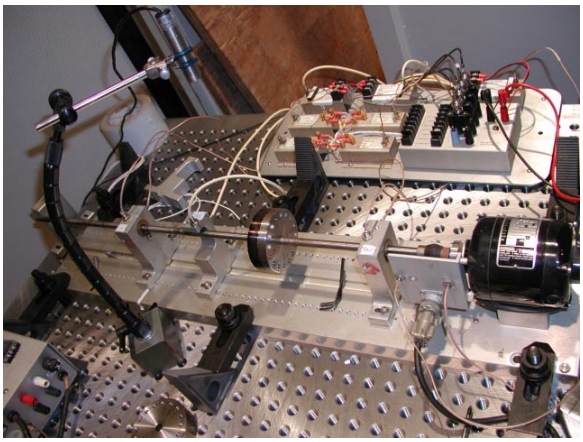

Figure 4-2.—BN RK 4 Rotor Kit

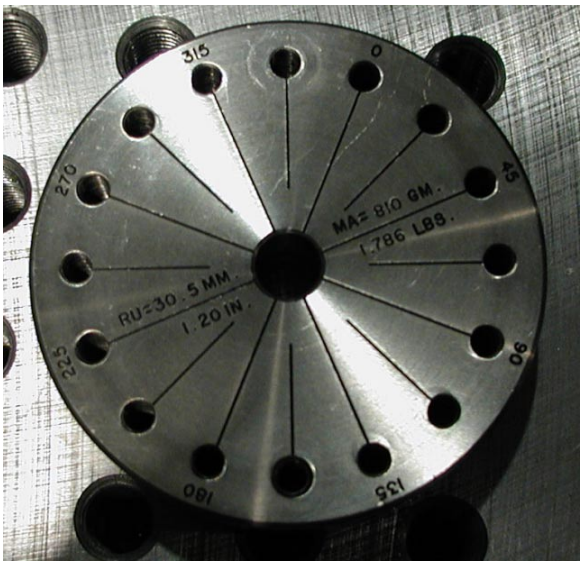

Figure 4-3.—Rotor kit Disk w/ Balance Slots.

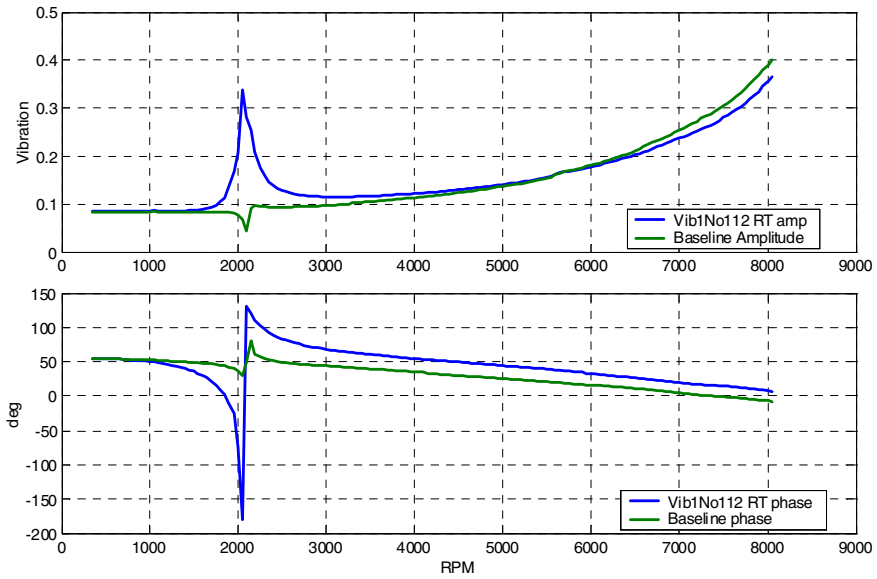

Figure 4-4.—Typical synchronous response, Vertical.

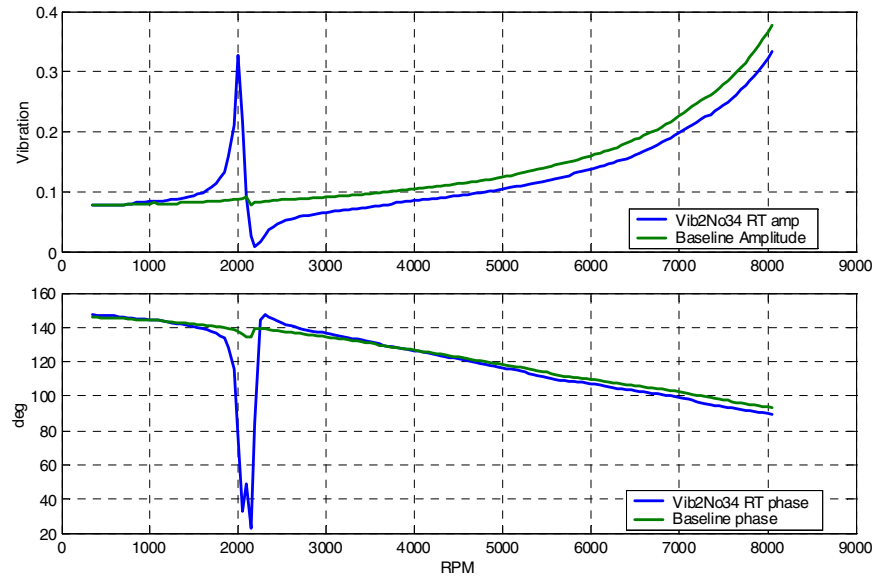

Figure 4-5.—Typical Synchronous Response, Horizontal

4.2 Tests

The initial system was not perfectly balanced. To verify the system integration and algorithms, unbalances were added at two circumferential positions: 0^o and 90^o on the rotor disk. The 1/rev signal comes from a notch on the shaft near the 0^o mark. The actual notch is a filing off of the shaft, which covers approximately 60^0 of circumference. According to the calibration, they correspond to

approximately 30° and 120° with respect to the 1/rev trigger. At each circumferential location, 4 different unbalance mounts were added: 1, 2, 3, and 4 set screws, which correspond to 3.416, 6.832, 10.248, and 13.664 g-mm unbalances.

The motor speed was controlled between 350 rpm to 8050 rpm. Twenty-five baseline runs were recorded. For each unbalance case, 5 runs were recorded for further analysis. The tests were repeated for 10 baseline conditions and 5 unbalanced runs for each unbalance case.

4.3 Data Reduction

4.3.1 Non-resonance based analysis

For non-resonant based analysis, the data in the speed range of 4000 to 4500 rpm were used. With this speed range, it satisfies $\frac{\omega_1}{\omega} \le 0.5$ and $\frac{\omega}{\omega_2} < 0.5$. First order approximation, Eq. (2-13), is used in this processing. Before curve fitting, the baseline response is subtracted from a real-time measurement in the complex domain. The difference is then used to carry out the complex domain curve fitting for extracting the mass unbalance coefficient and the crack induced unbalance coefficient. The magnitudes of the typical real time measurement, the baseline, and the difference are shown in Figure 4-6. As can be seen from the figure, in the difference signal, the "slow roll" effect introduced by the shaft geometric imperfection has been removed.

The curve fitting is carried out in the complex domain with least-square minimization of the difference between the raw data and the fitting curve in the specified RPM range. A typical example is shown in Figure 4-7.

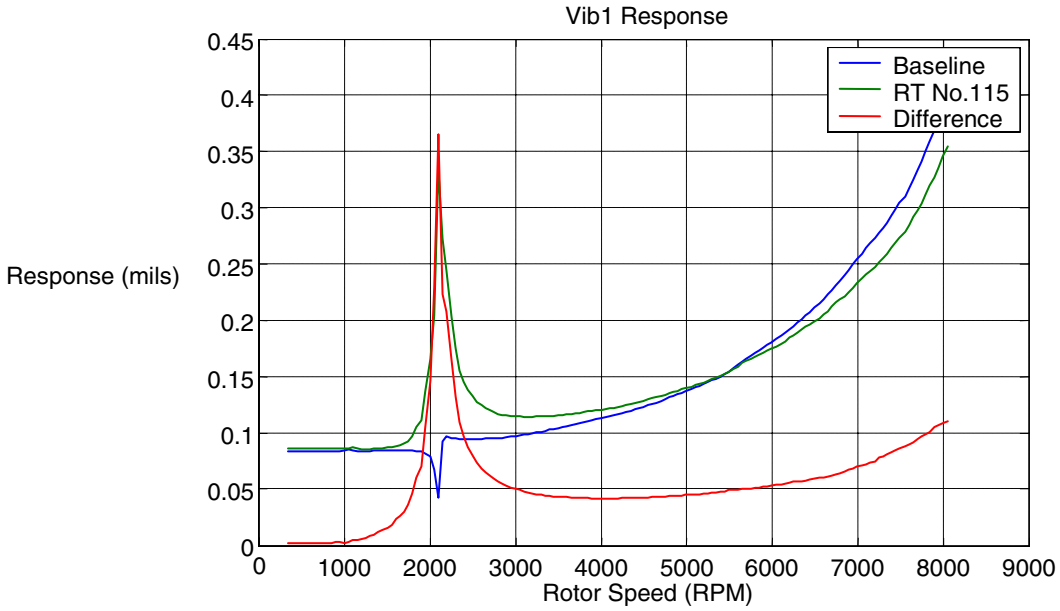

Figure 4-6.—A Typical Run: Real time measurement, baseline, and the difference.

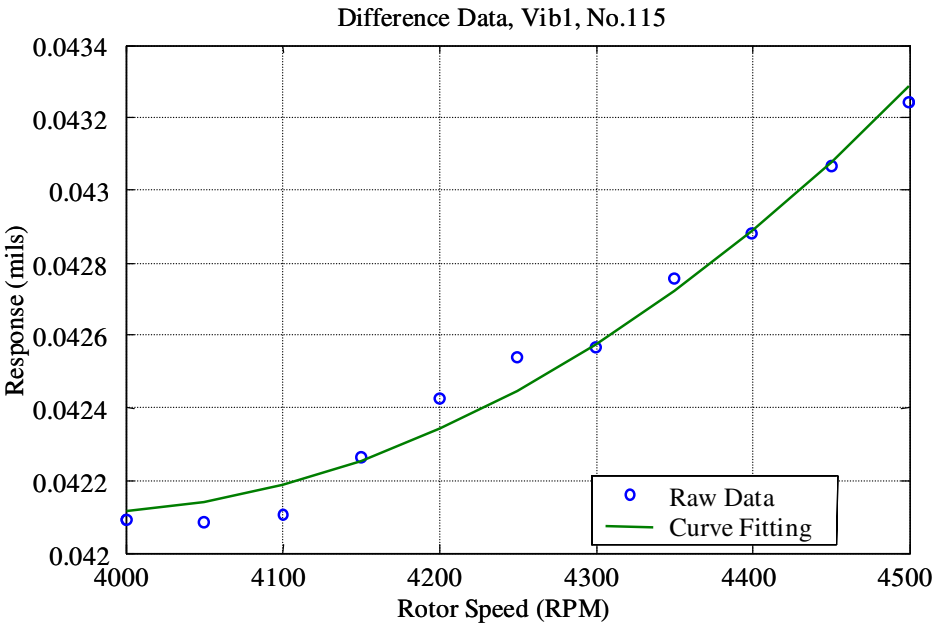

Figure 4-7.—Curve fitting results.

Figure 4- 8 shows the results from the vertical sensor, where C_0 is the mass unbalance indicator and C_2 is the crack induced unbalance indicator. This test contains a total of 115 runs. The first 25 runs are the baseline runs. In these runs, the system is balanced. The results are recorded for baseline constructions, i.e. the reference of the rotor health condition. The next 20 runs are the 0^o-unbalanced runs. One, 2, 3 and 4 nylon set crews were added to the 0^o mark on the rotor, respectively. For each unbalance case, five runs were repeated. The following 20 runs are the 90^o-unbalanced runs. In this case, the unbalance masses were removed from the 0^o location. One, 2, 3 and 4 nylon set crews were added to the 90^o mark on the rotor, respectively. For each unbalance case, five runs are repeated. To double-check the test, the procedure was repeated with 10 baseline runs, 20 0^o-unbalanced runs, and 20 90^o-unbalanced runs at different unbalance levels.

From Figure 4- 8, it is seen that that the mass unbalance indicator C_0 is proportional to the unbalance added, while the crack induced unbalance indicator C_2 does not have such trend. In Figure 4-9, the normalized C_0 and C_2 are shown for comparison. In the figure, C_0 is normalized with respect to the mean of the C_0 in the first 25 baseline runs, while C_2 is normalized with respect to the mean of the C_2 in the first 25 baseline runs. Again, the normalized C_0 is clearly proportional to the mass unbalance added. The crack induced unbalance indicator C_2 is small. In theory, C_2 should be a small constant. The slight increase could be due to fitting errors introduced by small terms.

To figure out the exact unbalance amount from C_0, the exact modal parameters, such as modal mass and mode shape, are required. To have a quick examination, the unbalance amount is normalized at the smallest unbalance at "0^o" and "90^o". Figure 4-10 shows the normalized mass unbalance identification. The corresponding error is shown in Figure 4-11. The identification error is less than 9% in this case.

Similar data processing was carried out on the horizontal sensor. The results are shown in Figure 4-12 to Figure 4-15. In this sensor, the fitting error is less than 6%.

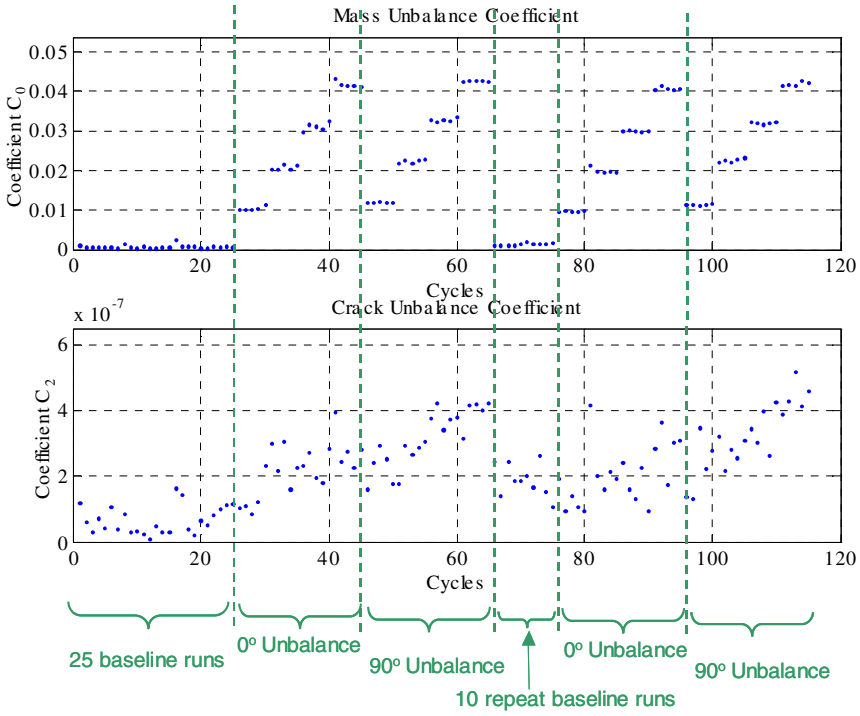

Figure 4- 8.—Non-resonance-based Analysis, Vertical sensor.

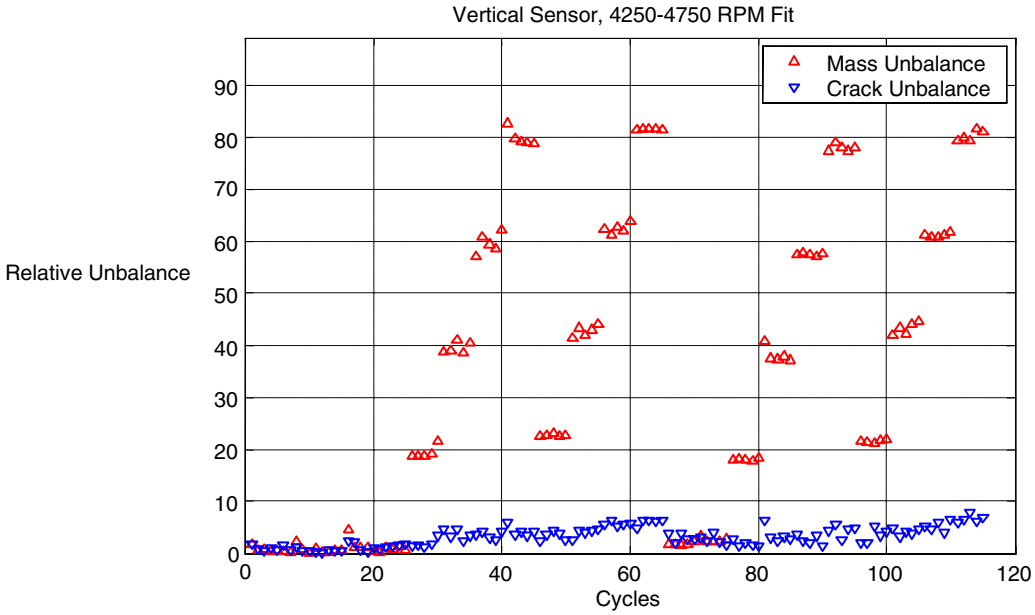

Figure 4- 9.—Identified unbalances normalized with respect to the averaged baseline values.

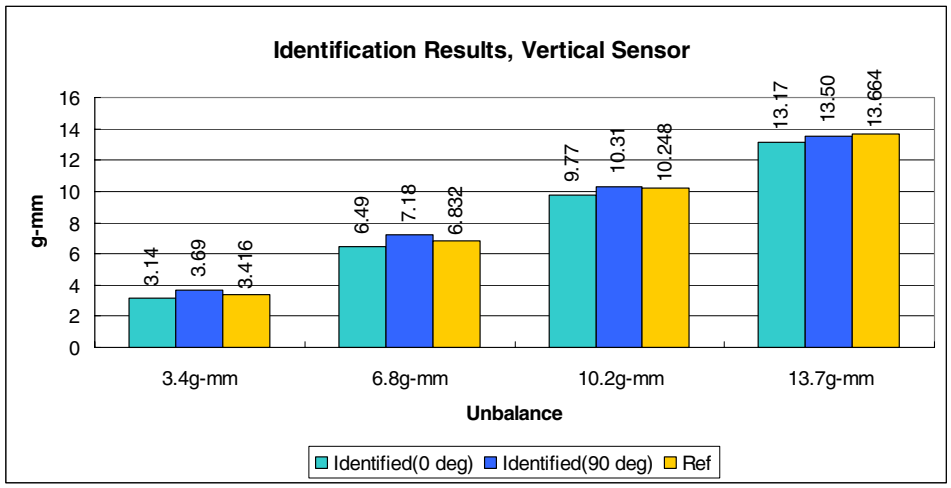

Figure 4-10.—Normalized Mass Unbalance Identification, Vertical Sensor.

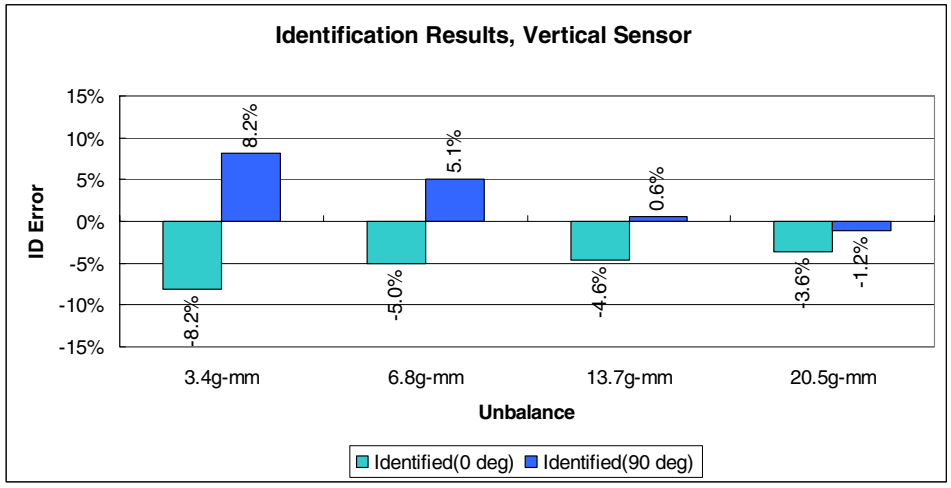

Figure 4-11.—Mass Unbalance Identification Relative Error, Vertical Sensor.

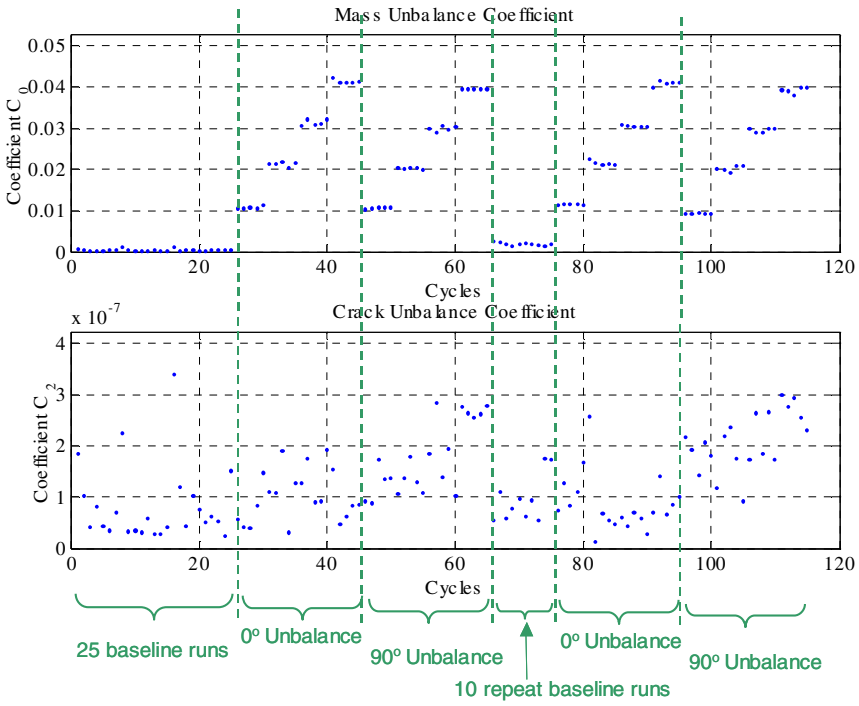

Figure 4-12.—Non-resonance-based Analysis, Horizontal sensor.

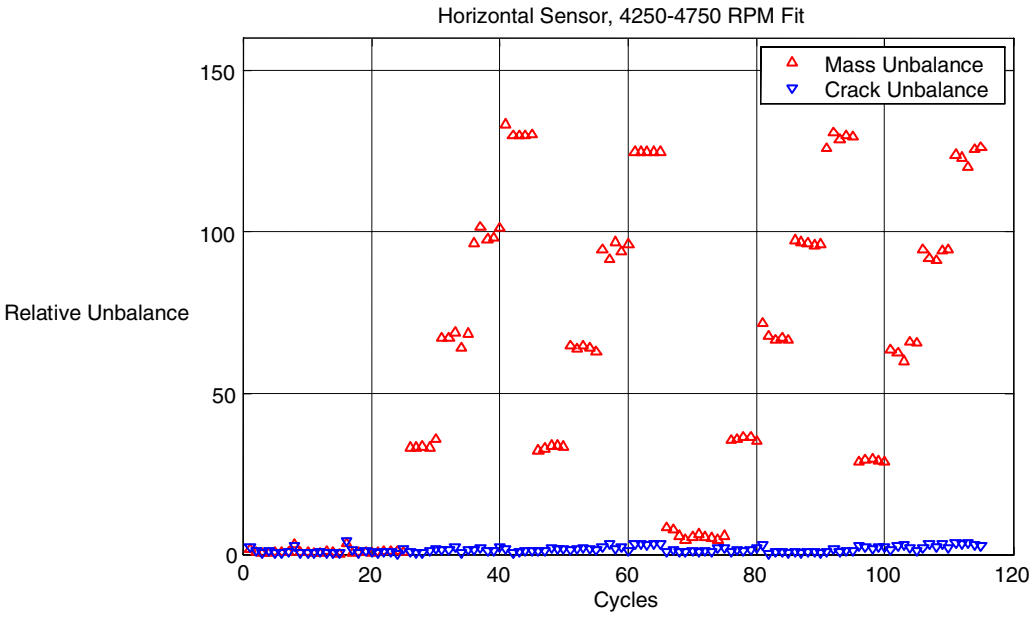

Figure 4- 13.—Identified unbalances normalized with respect to the averaged baseline values.

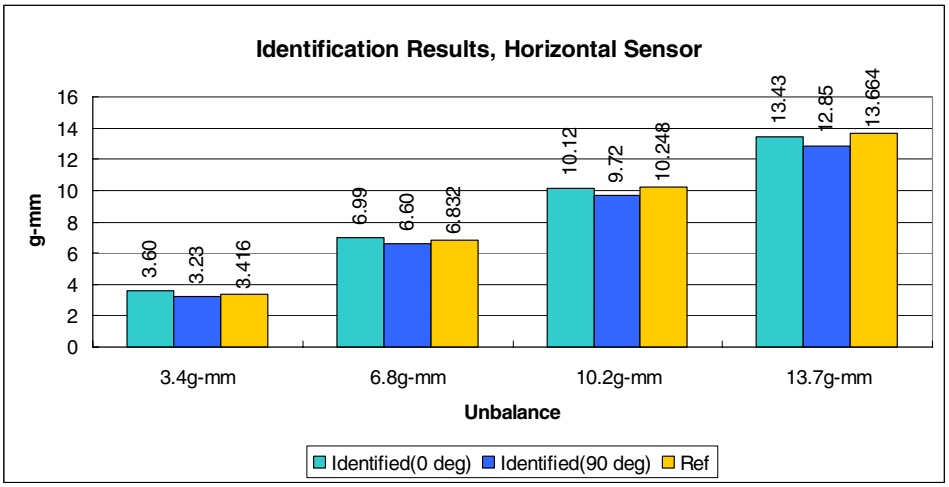

Figure 4-14.—Normalized Mass Unbalance Identification, Horizontal Sensor.

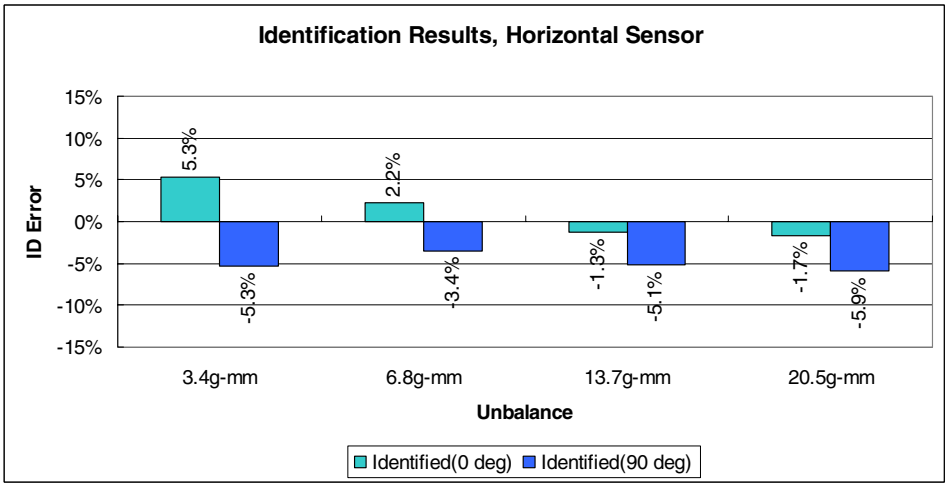

Figure 4-15.—Mass Unbalance Identification Relative Error, Horizontal Sensor.

4.3.2 Resonance based analysis

In the resonance-based analysis, the baseline is the complex average of the first 10 speed-up runs when the rotor is balanced. The baseline data are then removed from each real time data acquisition. The curve fitting is performed on the complex residue. The amplitude and phase of the mass unbalance are identified through curve fitting. Since the rotor shaft first bending is the dominant mode, a single-degree-freedom method is used, though multi-degree-freedom methods are also available.

Typical curve fitting results are shown in Figure 4-16. Usually, for the SDOF method, good curve-fitting results are achieved near the resonance in both amplitude and phase. The fitting parameter is a complex number (Figure 4-17); its amplitude is proportional to the additional unbalance relative to the baseline, while its phase indicates the circumferential location of the additional unbalance.

Figure 4-18 and Figure 4-19 show the unbalance amplitude and phase results from the vertical sensor curve fitting. It is seen that the amplitude identifications are approximately proportional to the added mass unbalance, while the phase identifications are very consistent at the same circumferential location. The standard deviation of phase identifications is 4.45° at "0° mass unbalance" and 2.95° at "90° mass unbalance". For the first 10 baseline runs, the amplitudes identified are small and the phases tend to be random, as expected.

Similar to the non-resonant situation, the modal parameters are not known. For quick comparison, the identified parameters are normalized with respect to the mass unbalance at "0°" and "90°" and the smallest unbalance amount: 3.416 g-mm. The averaged normalized amplitudes are shown in Figure 4-20. The amplitude identification relative error is shown Figure 4-21. For both circumferential locations, the relative fitting errors are less than 11%.

Similar data processing was carried out on the horizontal sensor. The results are shown in Figure 4-22 to Figure 4-25. Similar results are achieved. The relative fitting error was less than 9%.

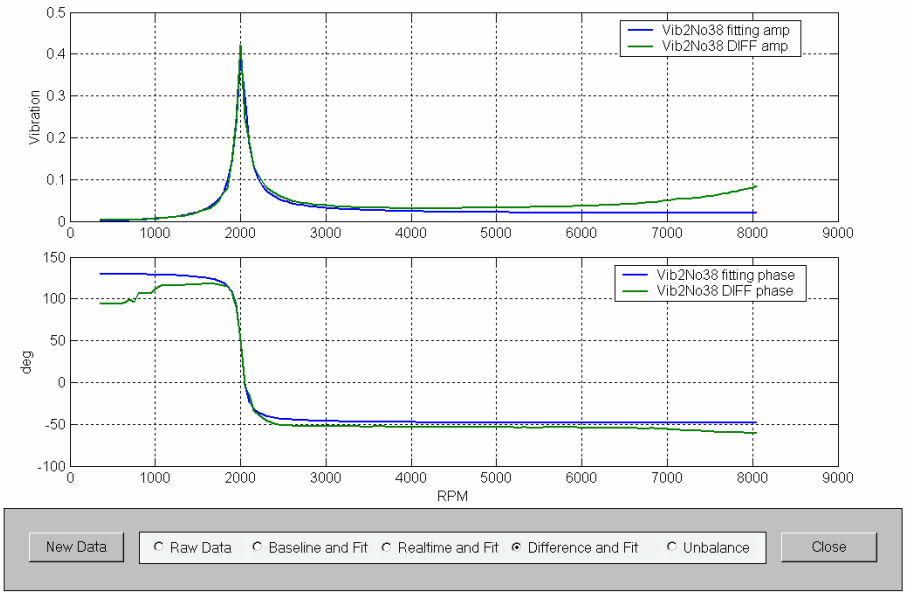

Figure 4-16.—SDOF Curve-fitting on the Complex Residue.

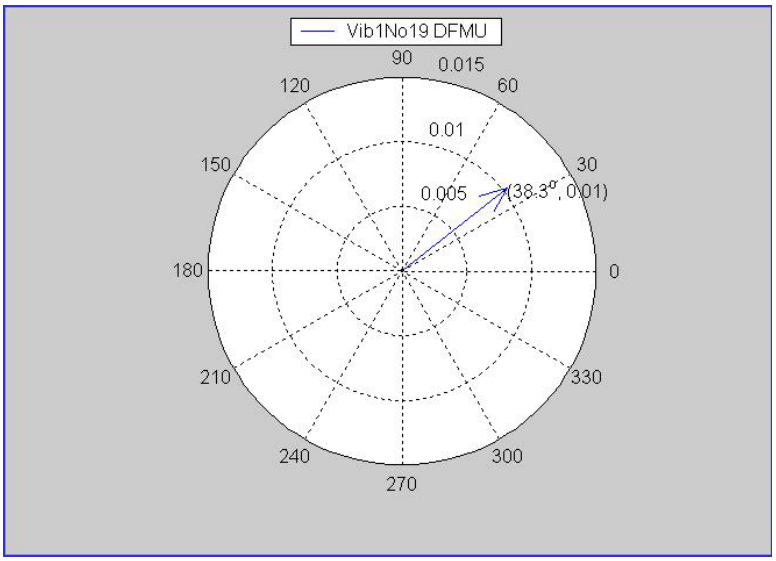

Figure 4-17.—Identified Vector.

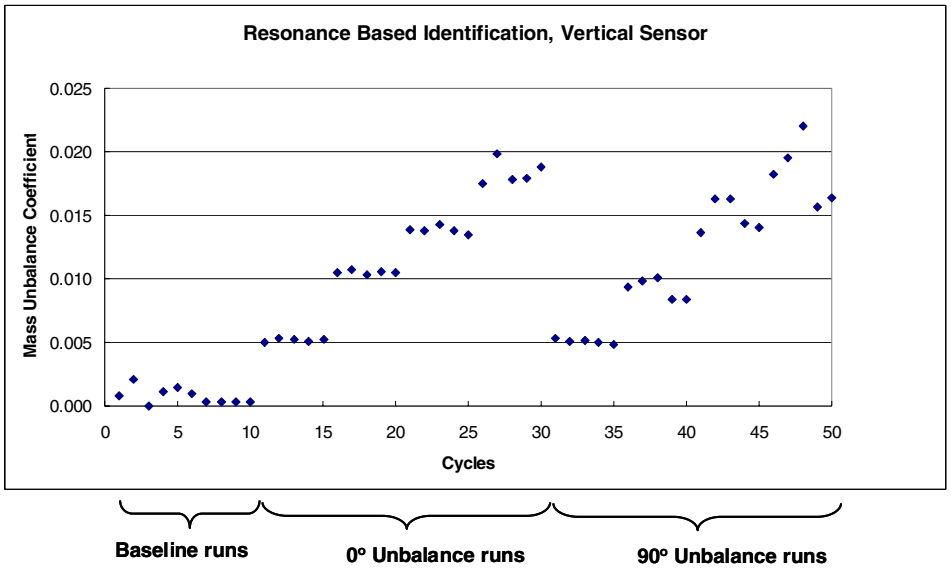

Figure 4-18.—Resonance-based Identification-Amplitude, Vertical Sensor.

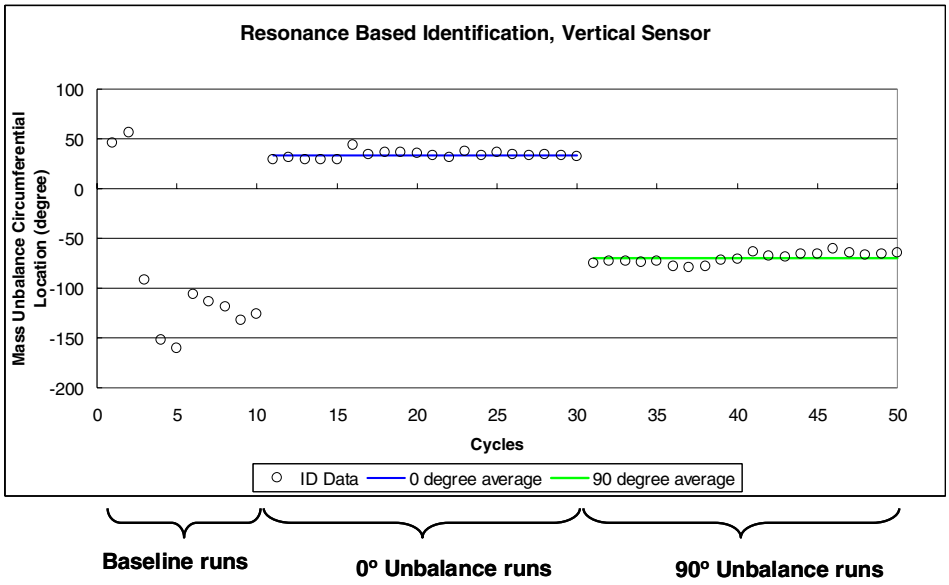

Figure 4-19.—Resonance-based Identification – Phase, Vertical Sensor.

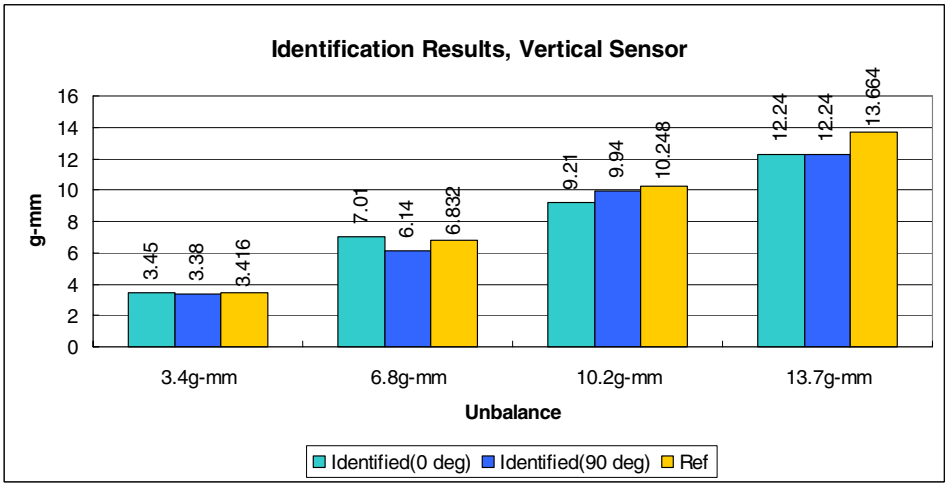

Figure 4-20.—Normalized ID Amplitude, Vertical Sensor.

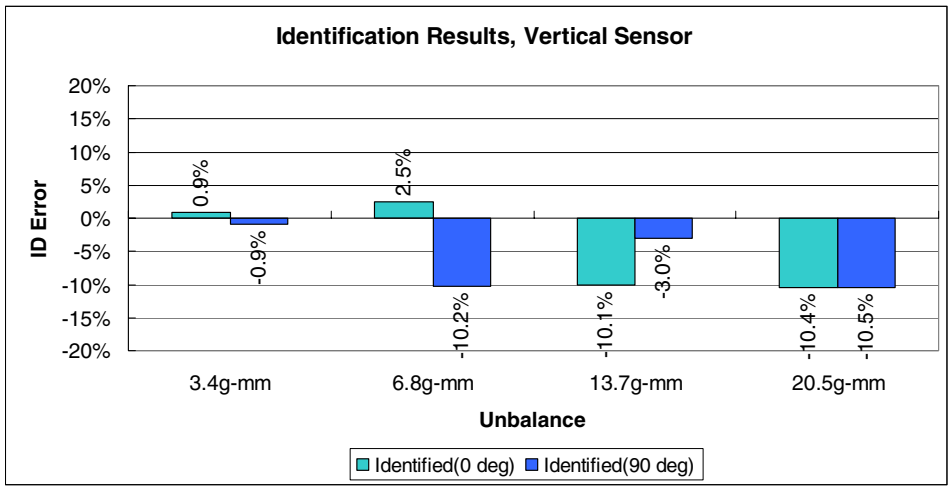

Figure 4-21.—Amplitude ID Relative Error, Vertical Sensor.

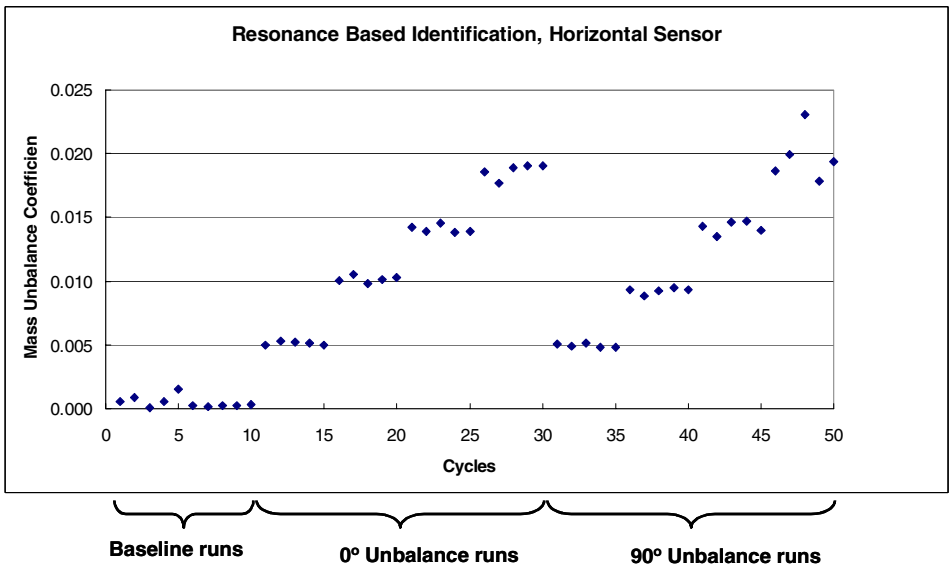

Figure 4-22.—Resonance-based Identification –Amplitude, Horizontal Sensor.

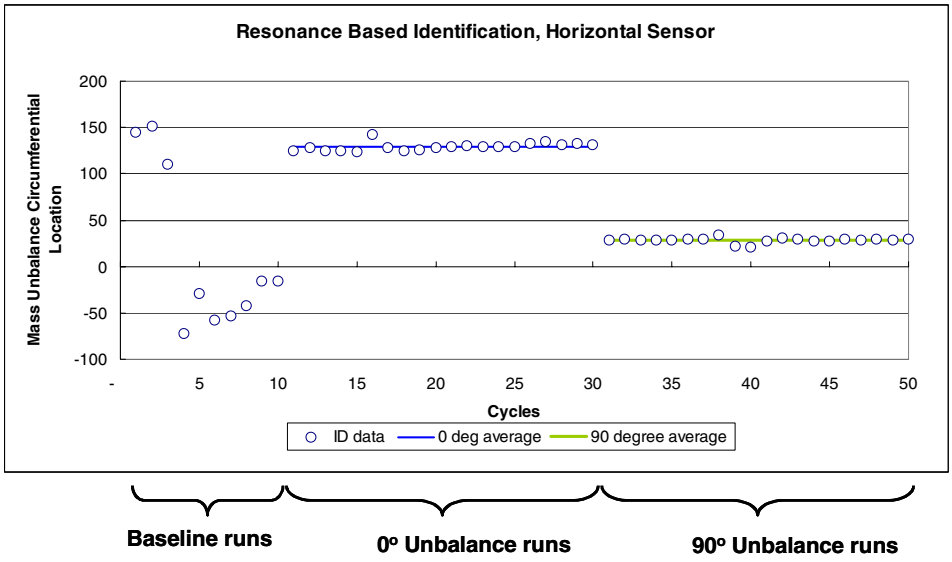

Figure 4-23.—Resonance-based Identification – Phase, Horizontal Sensor.

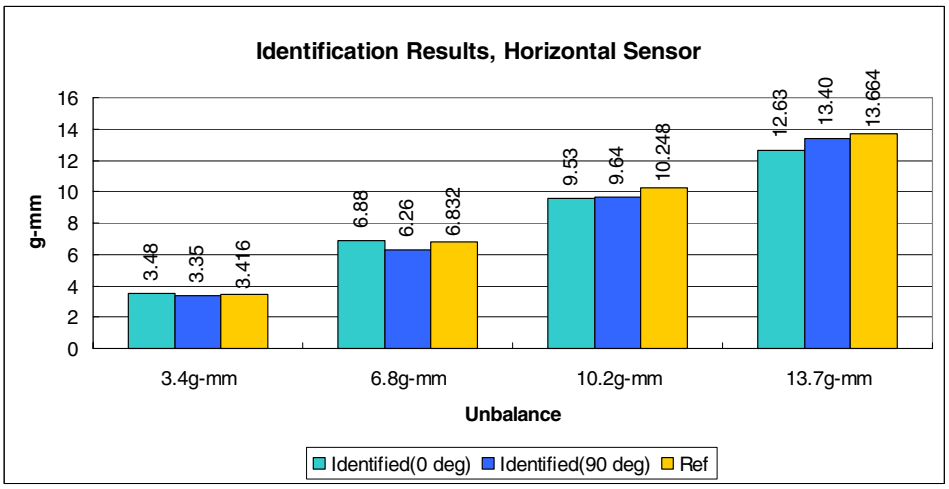

Figure 4-24.—Normalized ID Amplitude, Horizontal Sensor.

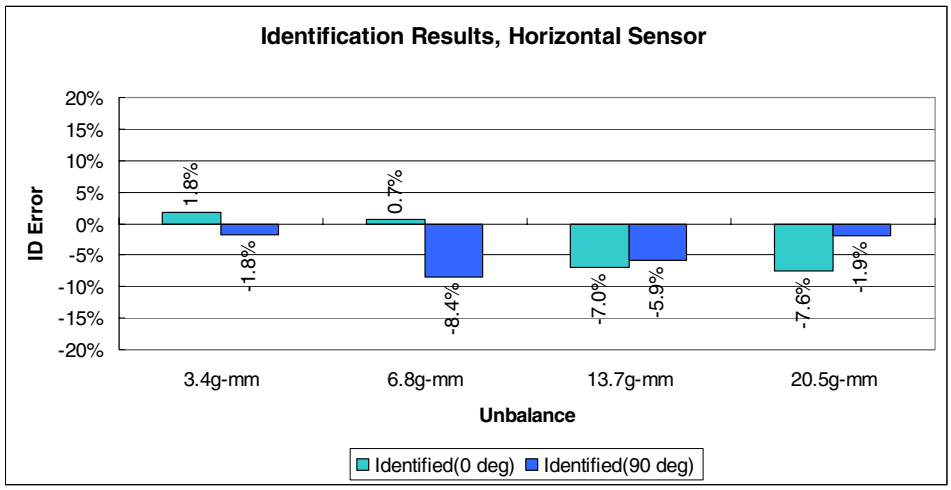

Figure 4-25.—Amplitude ID Relative Error, Horizontal Sensor.

4.4 Small Rotor Test Summary

The small rotor test successfully validated the system integration and proposed algorithms. The relative comparisons indicate that the identified mass unbalance coefficient, $C_{0,}$ is in agreement with the actual unbalances in magnitude. The crack coefficients are close to zero and do not show a correlation with respect to the mass unbalances. For the resonance-based algorithm, the method not only identified the amplitude of the mass unbalance, but the phase, or circumferential location, as well.

Generally, the resonance-based algorithm should have better identification accuracy than the non-resonance-based algorithm, because at resonance, the signal to noise ratio is usually higher. But in this well controlled rig test, this advantage is not shown (refer to Figure 4-11, Figure 4-15, and Figure 4-21,Figure 4-25). Careful inspection of the sensor responses indicates that there is a mode near the rotor first resonance, for which the response is not proportional to the mass unbalance. This mode is due to the support structure (see Figure 4- 26).

The resonance-based algorithm can be used in a health monitoring system for rotating machinery; it can also serve as an alternative for rotating machinery balancing.

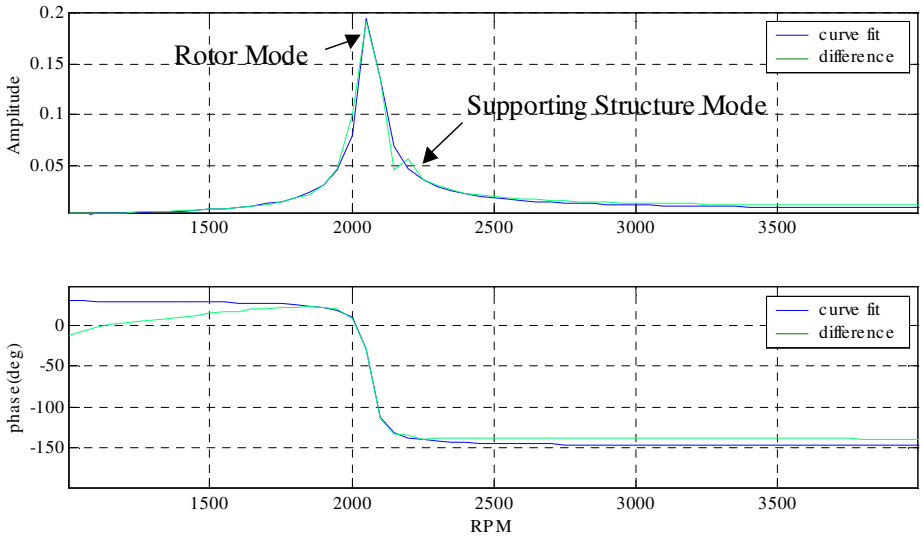

Figure 4- 26.—The supporting structure mode contaminated the rotor mode response.

5 Engine Test

The engine test was intended to demonstrate various crack detection strategies on an Allison TF41-A1B engine (see Figure 5-1). The GE system uses vibration sensors (accelerometers) mounted on the engine case. The detection algorithms introduced in Section 2 were implemented in the system integrated in Section 3 to detect crack propagation from the engine shaft synchronous vibration signature of the cracked disk. The advantage of this system is that the sensors used either already exist in an engine system or can be easily added.

The size and location for the initial fault seed was recommended by a prior stress analysis. It was determined that the location chosen was a high stress area and the size and location of the slot was conducive to crack propagation (refer to Figure 5-2).

The initial crack is an EDM flaw of 0.005” wide by 0.100” radius in the shape of a half penny notch into surface. The seeded fault was pre-cracked in a spin pit. Fluorescent penetrate (Figure 5-3) and eddy current (Figure 5-4) inspection techniques were performed[8]. The eddy current was believed to be more accurate. Eddy current inspection Figure 5-4 indicated 100 mils and 105 mils propagation at the corners of the initial crack[8].

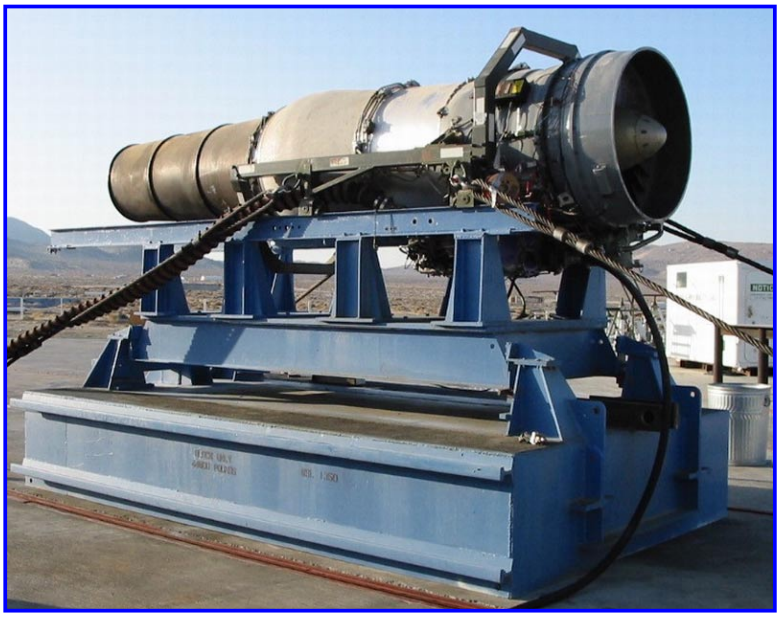

Figure 5-1.—Allison TF41-A1B Engine on Test Stand.

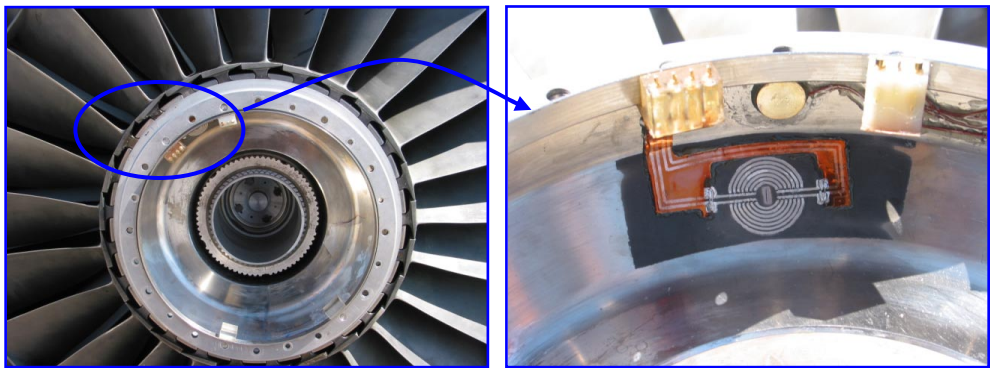

Figure 5-2.—Pre-cracked Fan Disk.

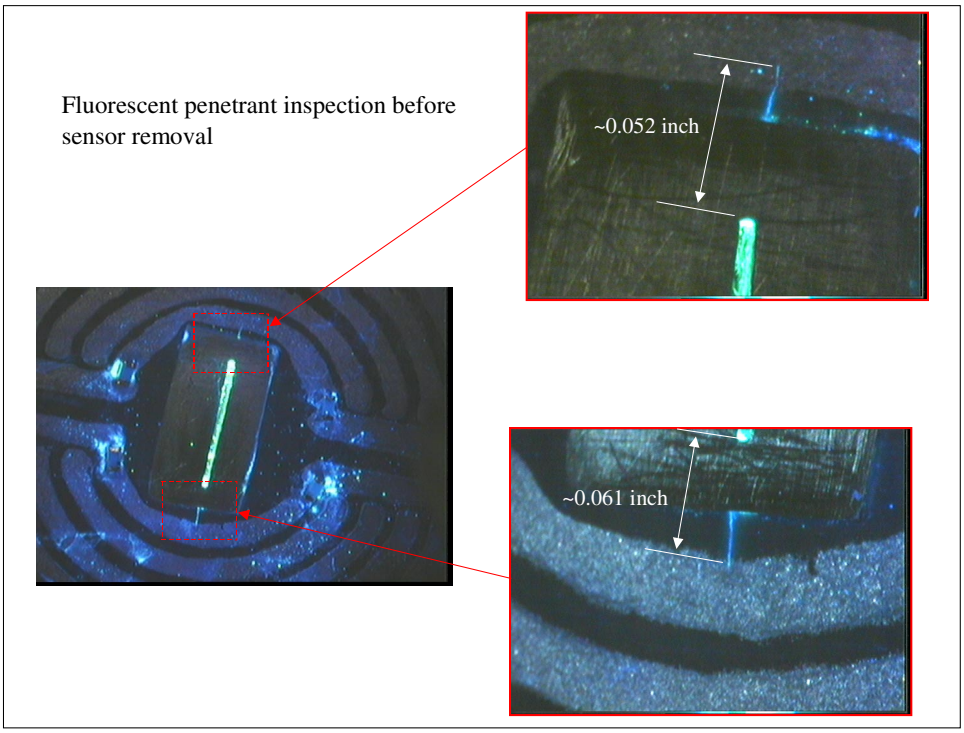

Figure 5-3.—Fluorescent Penetrant Inspection Results.

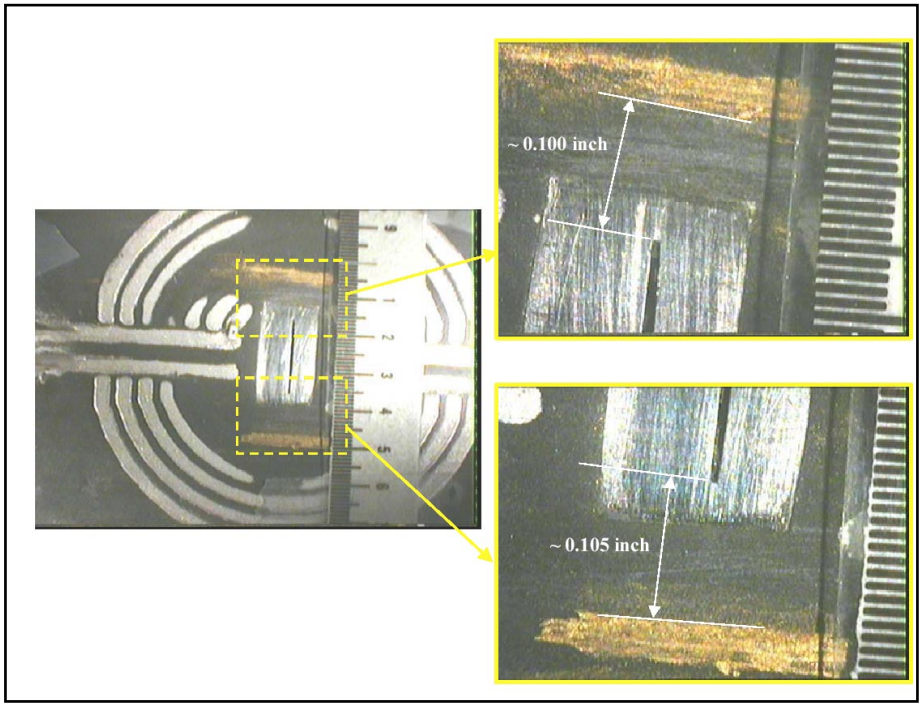

Figure 5-4.—Eddy Current Inspection Results.

5.1 Test setup

The GE system for this engine test uses four accelerometers as vibration sensors. The list of sensors is as follows:

- Sensor #1: PCB 353B32, SN 83106, sensitivity 51.0mv/g;
- Sensor #2: PCB353B32, SN 83107, sensitivity 51.1mv/g;
- Sensor #3: PCB 353B04, SN 81329, sensitivity 10.48mv/g;
- Sensor #4: PCB 353B04, SN 81330, sensitivity 10.33mv/g.

The sensors were mounted on the 1st stage stator case (Figure 5-5 and Figure 5-6), where the vibrations from the engine rotating parts can be best transmitted to the stationary engine case. Corresponding to the master sensor log (Figure 5-7 and Figure 5-8), sensor #1 is global list #8; Sensor #2 is global list #7; Sensor #3 is global list #10; and sensor #4 is global list #9.

The sensor signals were conditioned at the test pad. The signal conditioners were protected by a steel cabin to prevent potential damage by engine burst. The conditioned sensor signals were then transmitted to the control room for further on-line processing (Figure 5-9).

A 1/rev synchro-phasor and sensor and signals were also recorded by a TEAC 8-channel digital tape recorder for future off-line analysis as needed (Figure 5-9). The channel assignments are:

- Channel 1: 1/rev synchro-phasor, full-scale-value: 5volts;
- Channel 2: Accelerometer #1, full-scale-value: 20volts;
- Channel 3: Accelerometer #2, full-scale-value: 20volts;
- Channel 4: Accelerometer #3, full-scale-value: 20volts;
- Channel 5: Accelerometer #4, full-scale-value: 20volts;

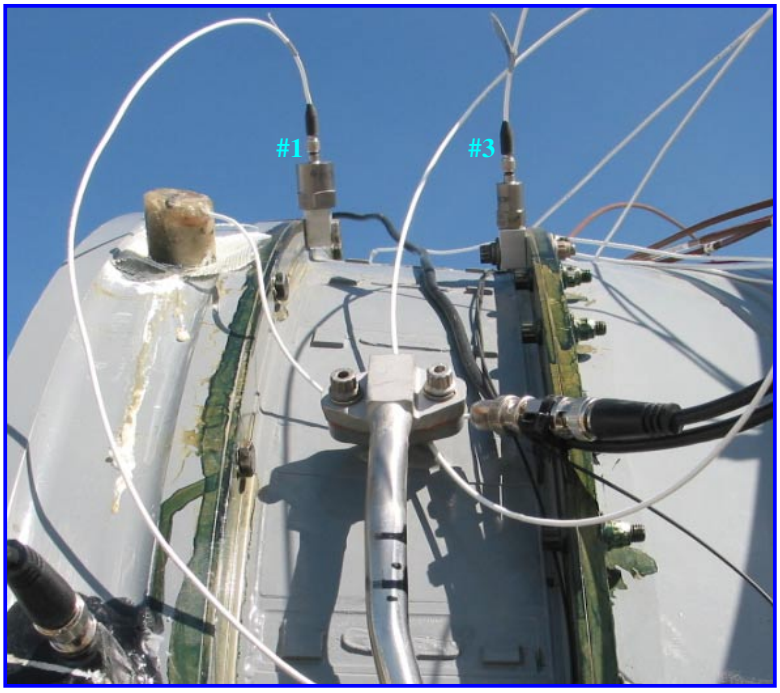

Figure 5-5.—Sensors #1 and #3.

Figure 5-6.—Sensors #2 and #4.

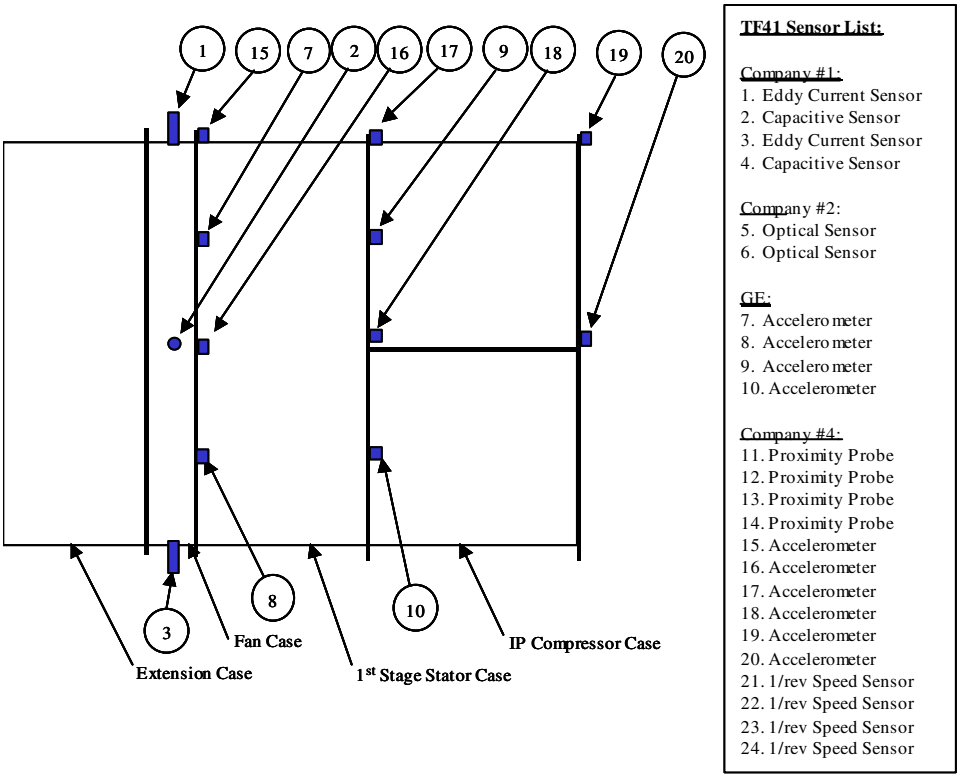

Figure 5-7.—Sensor Locations, Top view.

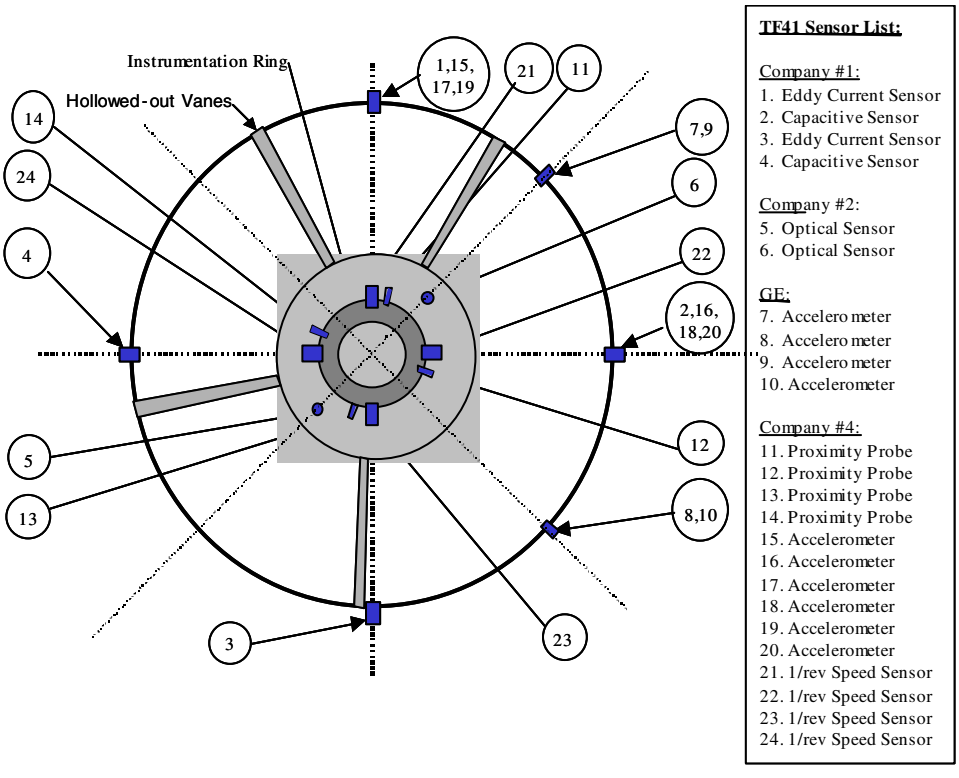

Figure 5-8.—Sensor Locations, Cross Section, Top On Right, Bottom On Left.

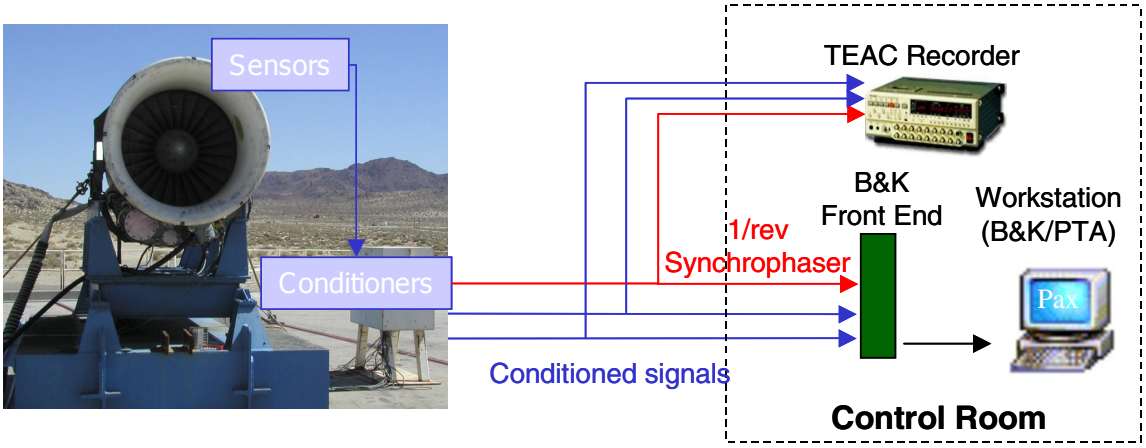

Figure 5-9.—Engine Test System Setup.

5.2 Data Processing

The engine test started on March 24, 2003. The initial cycle profile was set as 27 short cycles plus one long cycle every one half hour. The short and long cycles are defined as:

- The longer cycles consisted of a 30 second dwell at idle, 75 second ramp to maximum speed (8000 rpm), 30 second dwell at maximum speed, and a 15 second ramp to idle (approximately 2500 rpm) for a total cycle time of 150 seconds.
- The shorter cycle consisted of a 15 second dwell at idle, a 15 second ramp to maximum speed (8000 rpm), a 15 second dwell at maximum speed, and a 15 second ramp to idle (2500 rpm) for a total cycle time of 60 seconds.

After the first day test, all the systems participating found no indication of crack propagation. To increase the crack growth rate, the team decided to increase the maximum speed to 8900 rpm on March 25. The GE system consequently changed the speed region from 2750-8050 rpm to 3450- 8750 rpm. As a result, the first 380 cycles will not be included in the signal processing.

The two-week's test finished with more than 4700 cycles without an engine burst and without solid indication of crack propagation.

A typical rotor synchronous vibration response is shown in Figure 5-10, where the blue line is the amplitude of the baseline, which was constructed in the beginning of the test by averaging 30 runs. The green line is the amplitude of a real time run, while the red line is the amplitude of the complex difference between the real time response and the baseline. Since the resonant structure was unknown at the beginning, the non-resonant method was chosen for health monitoring during the real time test.

The non-resonant curve fitting in the full speed range (3500 to 8600 RPM) are shown in Figure 5-11. The upper portion of the figure is a real time measurement and the corresponding curve fitting. The middle portion is the baseline and its curve fitting. The lower portion shows the difference between the

real time data and the baseline, and the corresponding curve fitting. The parameters from the difference data curve fitting were used for health monitoring. Figure 5-12 to Figure 5-15 show the results of the full speed range (3500 to 8600 RPM) analyses, where C_0 is an indicator of mass unbalance and C_2 is an indicator of crack-induced unbalance.

Since, in general, the unbalance induced vibrations are higher at the higher rotational speed, another analysis, this one focused on high speed (7000 to 8600 RPM), was also conducted off-line. The curve fitting results are shown in Figure 5-16 to Figure 5-20.

Off-line 2/rev data analysis indicated that the engine system has significant resonance frequencies around 10000RPM (Figure 5-21), thus non-resonance curve-fitting method at high RPM, say above 8000RPM, is not the best choice. The curve fitting at low RPM region (3500 to 4500RPM) was carried out, and the results are shown in Figure 5-22 to Figure 5-26.

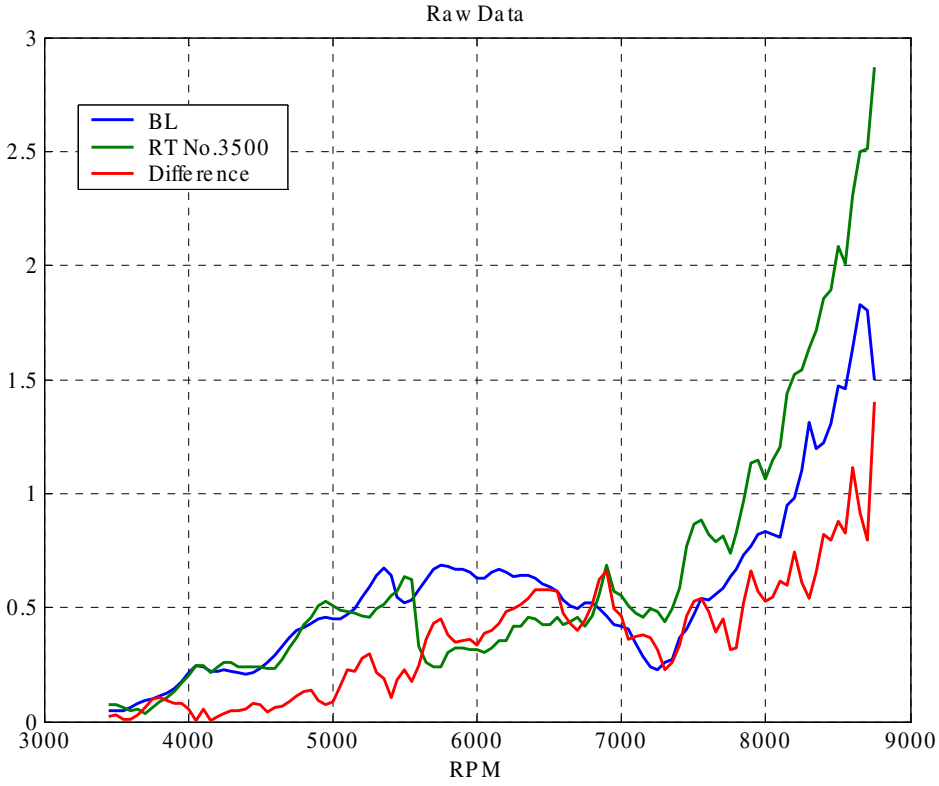

Figure 5-10.—A typical synchronous vibration response.

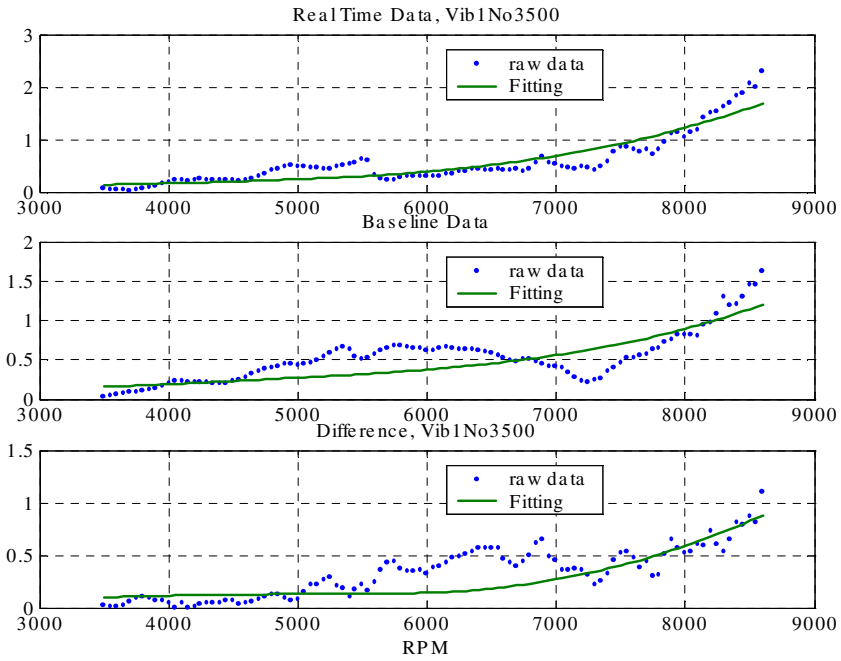

Figure 5-11.—A typical curve fitting.

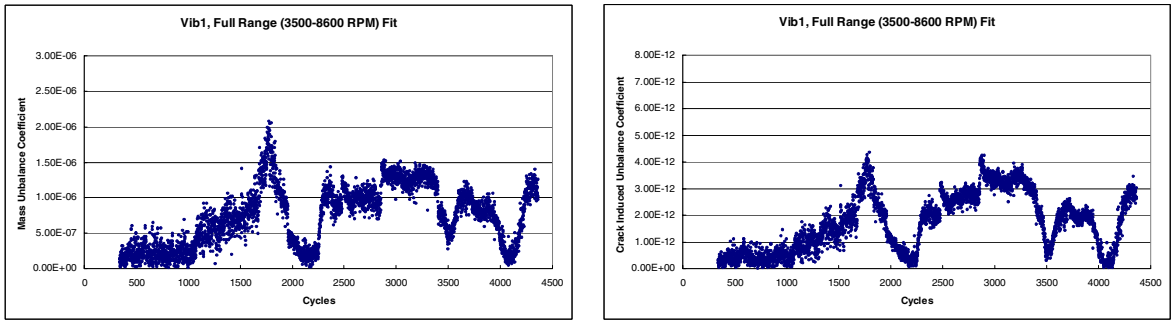

(a) Mass unbalance coefficient (b) Crack induced unbalance coefficient

Figure 5-12.—Sensor #1 Results, 3500-8600RPM.

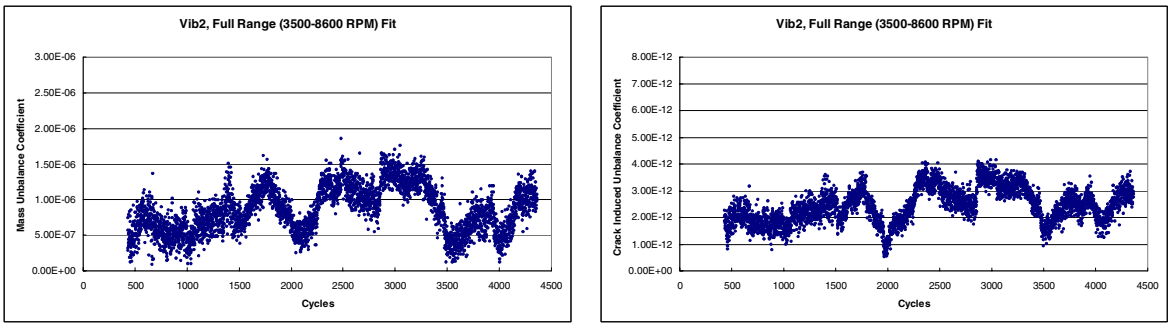

(a) Mass unbalance coefficient (b) Crack induced unbalance coefficient

Figure 5-13.—Sensor #2 Results, 3500-8600RPM.

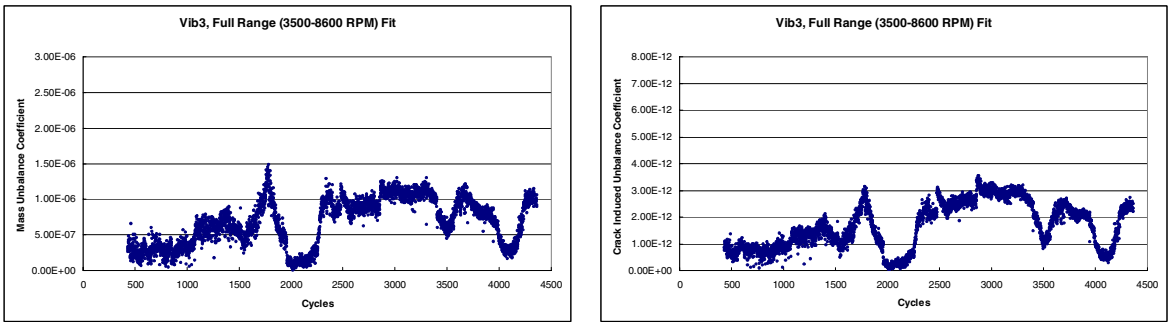

(a) Mass unbalance coefficient (b) Crack induced unbalance coefficient

Figure 5-14.—Sensor #3 Results, 3500-8600RPM

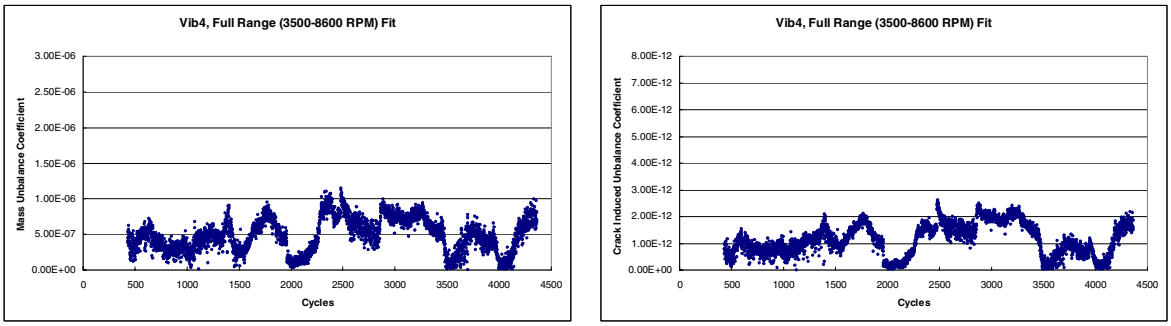

(a) Mass unbalance coefficient (b) Crack induced unbalance coefficient

Figure 5-15.—Sensor #4 Results, 3500-8600RPM.

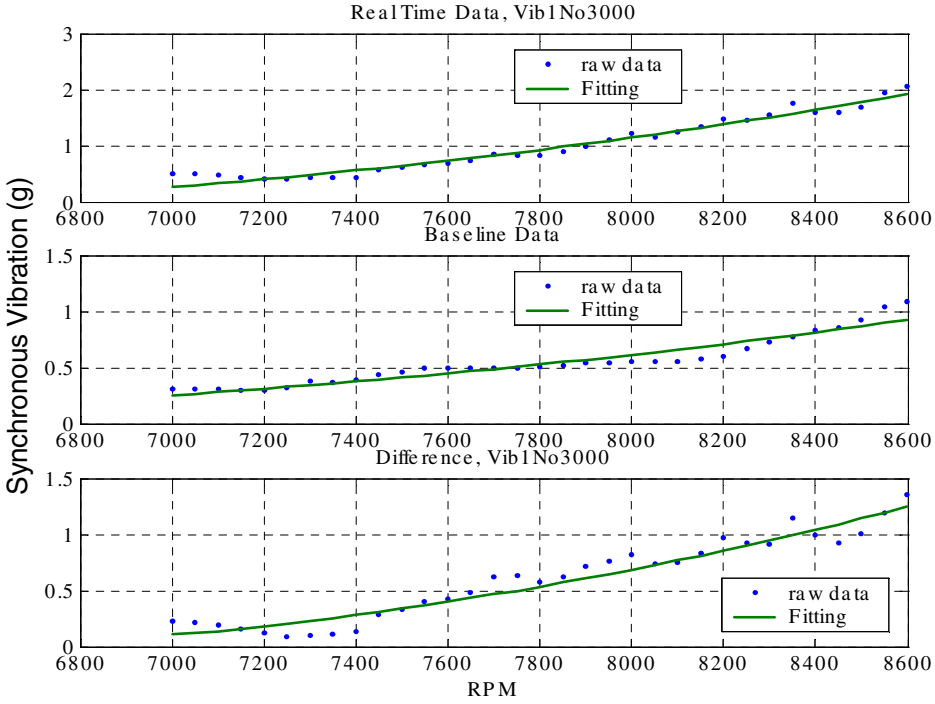

Figure 5-16.—A typical curve fitting in the high speed range.

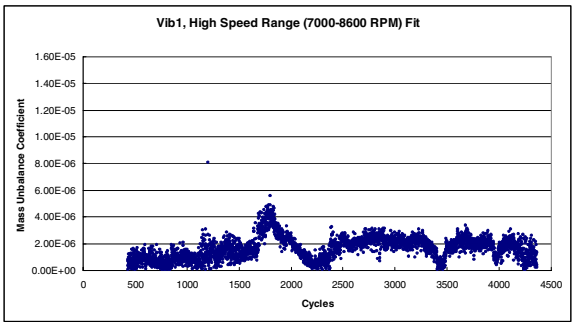

(a) Mass unbalance coefficient

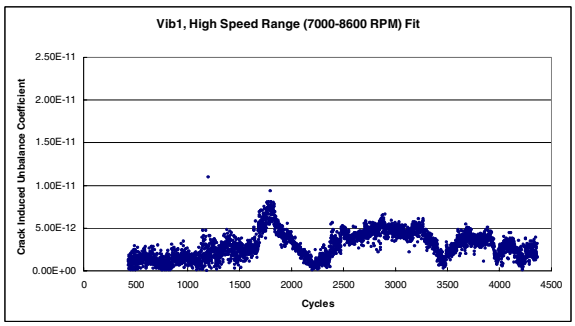

(b) Crack induced unbalance coefficient

Figure 5-17.—Sensor #1 Results, 7000-8600 RPM.

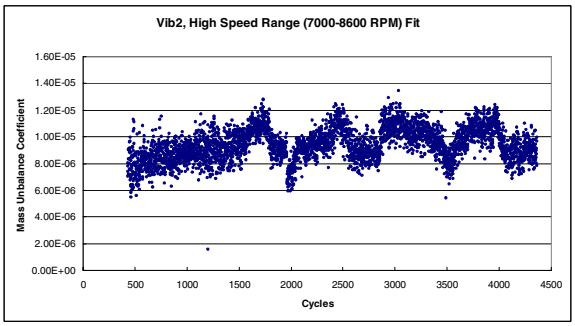

(a) Mass unbalance coefficient

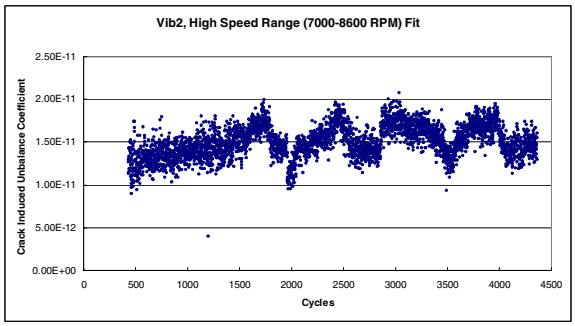

(b) Crack induced unbalance coefficient

Figure 5-18.—Sensor #2 Results, 7000-8600 RPM.

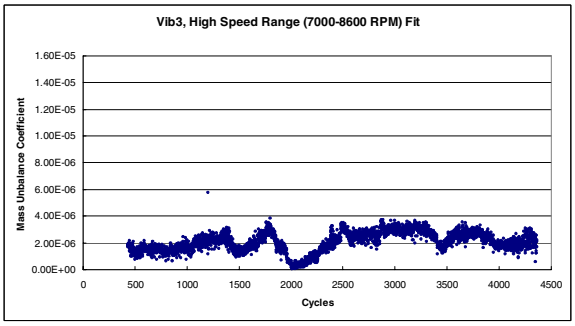

(a) Mass unbalance coefficient

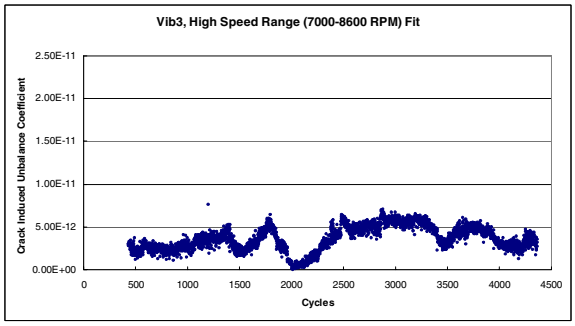

(b) Crack induced unbalance coefficient

Figure 5-19.—Sensor #3 Results, 7000-8600 RPM.

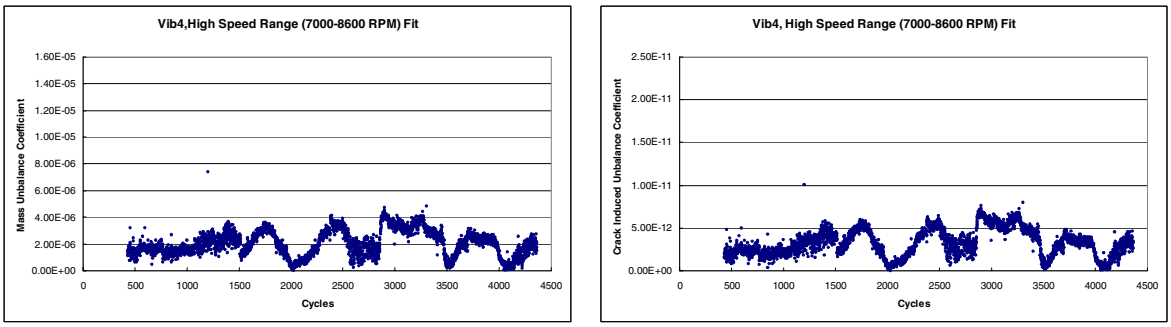

(a) Mass unbalance coefficient (b) Crack induced unbalance coefficient

Figure 5-20.—Sensor #4 Results, 7000-8600 RPM.

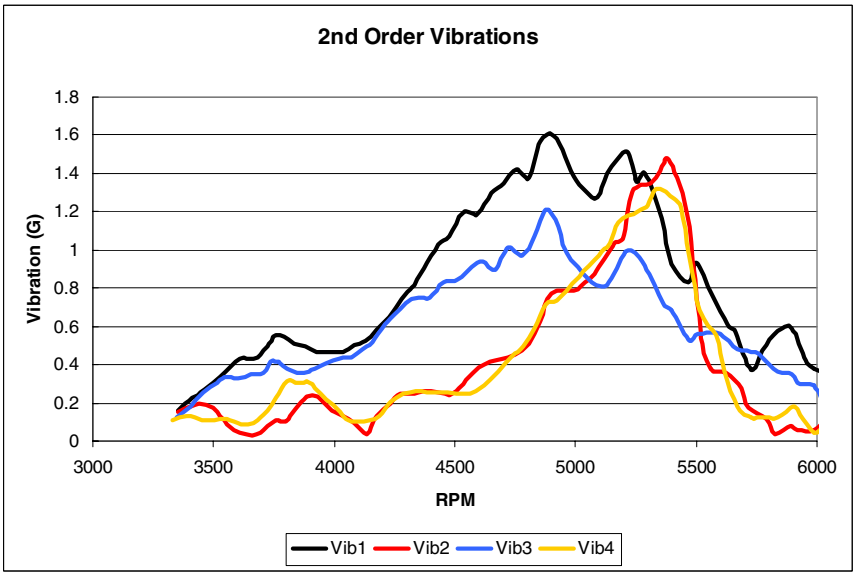

Figure 5-21.—2/rev data indicate resonance around 10000 RPM.

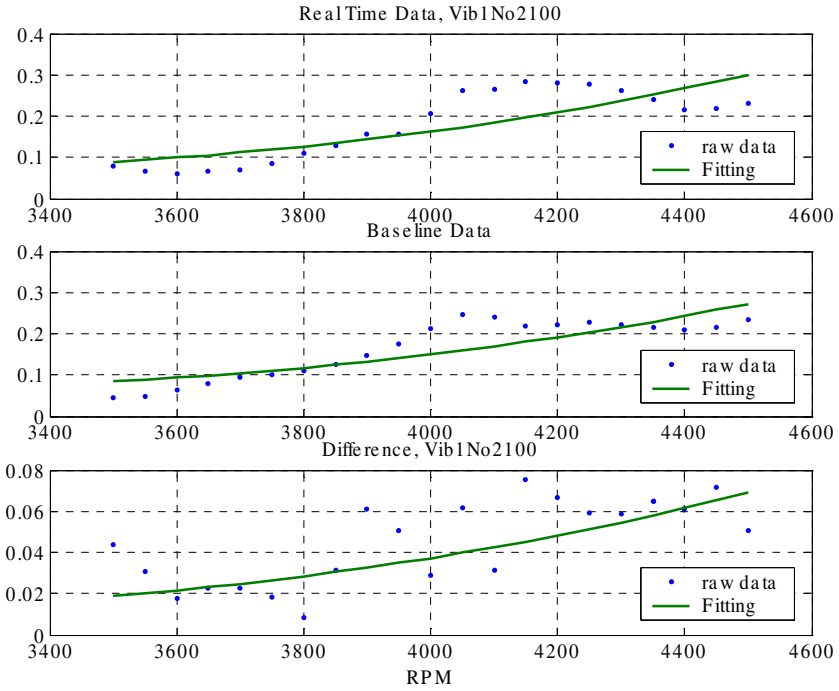

Figure 5-22.—A typical curve fitting in the low speed range.

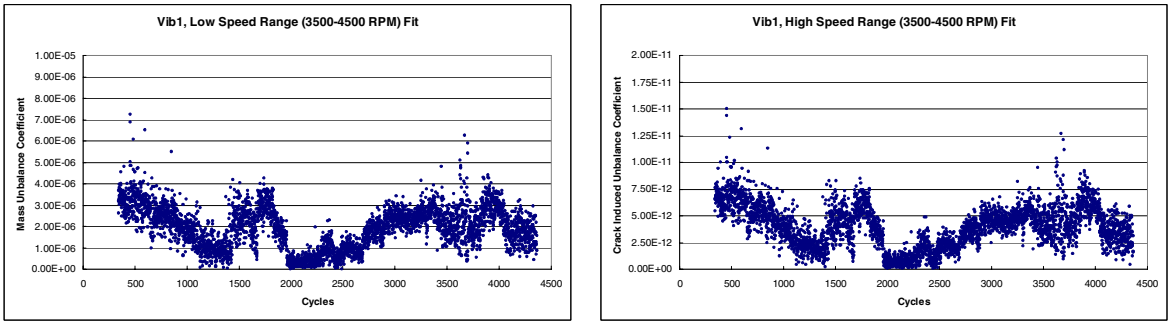

(a) Mass unbalance coefficient (b) Crack induced unbalance coefficient

Figure 5-23.—Sensor #1 Results, 3500-4500 RPM.

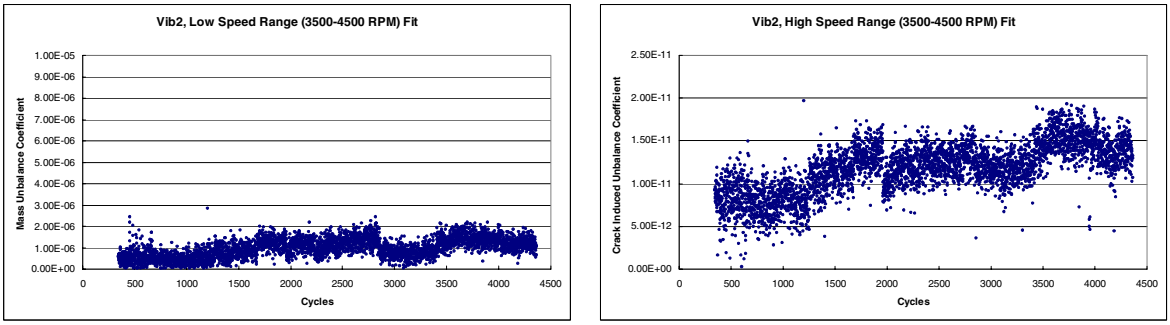

(a) Mass unbalance coefficient (b) Crack induced unbalance coefficient

Figure 5-24.—Sensor #2 Results, 3500-4500 RPM.

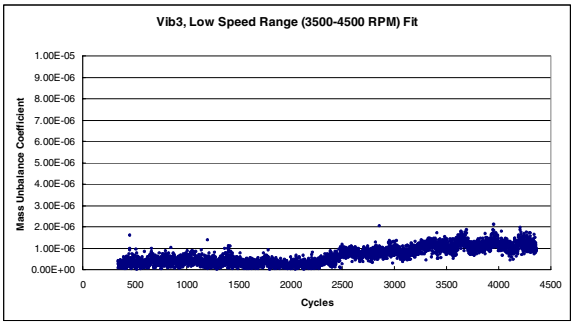

(a) Mass unbalance coefficient

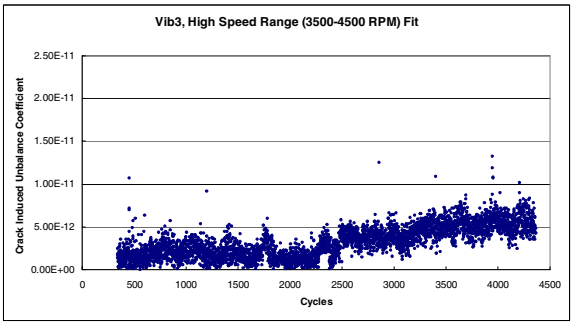

(b) Crack induced unbalance coefficient

Figure 5-25.—Sensor #3 Results, 3500-4500 RPM.

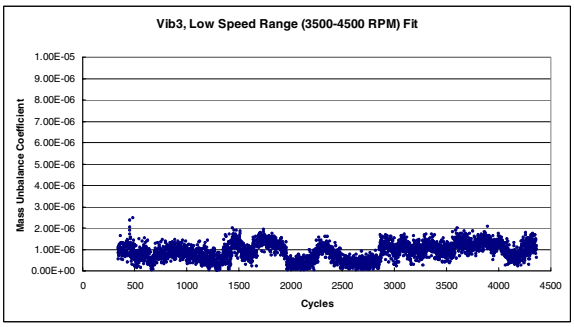

(a) Mass unbalance coefficient

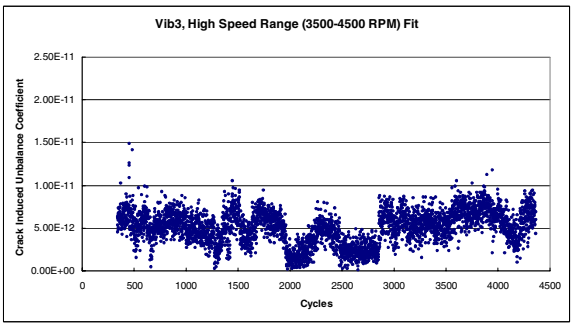

(b) Crack induced unbalance coefficient

Figure 5-26.—Sensor #4 Results, 3500-4500 RPM.

5.3 Summary

With the high speed range curve fitting, the fitting residues are smaller (Compare Figure 5-11, Figure 5-16, and Figure 5-22), due to better signal to noise ratio in the high speed range. But full speed range, high speed range, and low speed curve fittings showing similar results: there is no consistent trend in either the mass unbalance coefficient or the crack induced unbalance coefficient. The minor changes in the coefficients with respect to the cycle numbers are mainly due to day-to-day variations and random errors from data acquisition and curve fitting. No significant crack propagation or mass unbalance accumulation has happened during the two-week test.

6 Conclusions and Recommendations

Based on the test data analyses, the GE system indicated that after the two week test, the seeded fan disk flaw did not propagate enough to be detected by changes in the synchronous vibration. Mass unbalance accumulation was not detected either. The day-to-day operation variance and random variations are the major response in the system.

The GE team recommends the continuation of the test in the future if possible. In the 2nd order synchronous vibration analysis, major peaks appeared around 5000RPM (Figure 6-1), which implies there are resonances around 10000RPM in the synchronous vibrations. As a result, the speed range far away from the resonance condition is not perfectly satisfied in the first order analysis. Thus, we also recommend that prior to the test, a quick modal analysis be done to identify the exact modal parameters of these resonances so that the resonance-vibration based identification method can be applied. We believe this method has better accuracy in detection.

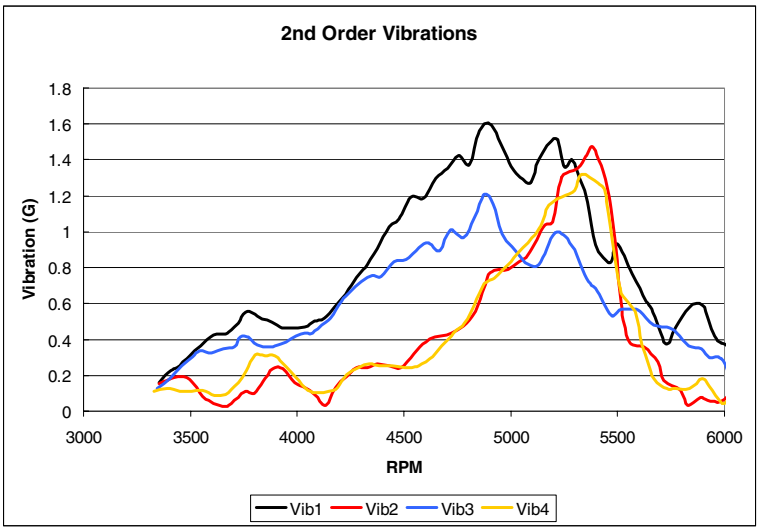

Figure 6-1.—2nd Order Synchronous Vibrations.

7 References

1 Thomson W.T. and Dahleh, M.D., *Theory of Vibration with Applications*, 5th Ed., Prentice-Hall, Englewood Cliffs, New Jersey (1998).

2 Tada H., Paris P., and Irwin, G., *The Stress Analysis of Cracks Handbook*, 2nd Ed., Del Research Corp., St. Louis, Missouri (1985).

3 NASA TM X-73307, *Astronautics Structures Manual, Vol. III* (1975).

4 Mark G. Butz and Hector Rodriguez, *Propulsion Health Monitoring for Enhanced Safety*, NASA Contract NAS3-99203

5 Hector Rodriguez, Darren Hallman, Mark Butz, and Vikas Dhar, *A physics-based approach for the detection of cracks in rotating Disks*, XV ISABE (2001).

6 Imdad Imam and Horst G. DeLorenzi, *Method and apparatus for detecting axial cracks in rotors for rotating machinery*, United States Patent #4,751,657, June 14, 1988.

7 H. Eric Sonnichsen and Borislav Milatovic, *Detecting anomalies in rotating components*, United States Patent #6,098,022, August 1, 2000.

8 John C. Brausch, TF-41 Test Rotor Evaluation Report, 43493TA0/PLSS, March 25, 2003

REPORT DOCUMENTATION PAGE

Form Approved
OMB No. 0704-0188

1. AGENCY USE ONLY (*Leave blank*)	2. REPORT DATE	3. REPORT TYPE AND DATES COVERED
	May 2004	Final Contractor Report

4. TITLE AND SUBTITLE

Disk Crack Detection for Seeded Fault Engine Test

5. FUNDING NUMBERS

WBS–22–728–30–03
NAS3–01135, Task 7

6. AUTHOR(S)

Huageng Luo, Hector Rodriguez, Darren Hallman, and Dennis Corbly

7. PERFORMING ORGANIZATION NAME(S) AND ADDRESS(ES)

GE Global Research
1 Research Circle
Niskayuna, New York 12309

8. PERFORMING ORGANIZATION REPORT NUMBER

E–14545

9. SPONSORING/MONITORING AGENCY NAME(S) AND ADDRESS(ES)

National Aeronautics and Space Administration
Washington, DC 20546–0001

10. SPONSORING/MONITORING AGENCY REPORT NUMBER

NASA CR—2004-213069

11. SUPPLEMENTARY NOTES

Huageng Luo, Hector Rodriguez, and Darren Hallman, GE Global Research, 1 Research Circle, Niskayuna, New York 12309; and Dennis Corbly, GE Aircraft Engines, 1 Neumann Way, Cincinnati, Ohio 45215–1988. Project Manager, David G. Lewicki, Structures and Acoustics Division, NASA Glenn Research Center, organization code 5950, 216–433–3970.

12a. DISTRIBUTION/AVAILABILITY STATEMENT

Unclassified - Unlimited
Subject Category: 37 Distribution: Nonstandard

Available electronically at http://gltrs.grc.nasa.gov

This publication is available from the NASA Center for AeroSpace Information, 301–621–0390.

12b. DISTRIBUTION CODE

13. ABSTRACT ***(Maximum 200 words)***

Work was performed to develop and demonstrate vibration diagnostic techniques for the on-line detection of engine rotor disk cracks and other anomalies through a real engine test. An existing single-degree-of-freedom non-resonance-based vibration algorithm was extended to a multi-degree-of-freedom model. In addition, a resonance-based algorithm was also proposed for the case of one or more resonances. The algorithms were integrated into a diagnostic system using state-of-the-art commercial analysis equipment. The system required only non-rotating vibration signals, such as accelerometers and proximity probes, and the rotor shaft 1/rev signal to conduct the health monitoring. Before the engine test, the integrated system was tested in the laboratory by using a small rotor with controlled mass unbalances. The laboratory tests verified the system integration and both the non-resonance and the resonance-based algorithm implementations. In the engine test, the system concluded that after two weeks of cycling, the seeded fan disk flaw did not propagate to a large enough size to be detected by changes in the synchronous vibration. The unbalance induced by mass shifting during the start up and coast down was still the dominant response in the synchronous vibration.

14. SUBJECT TERMS	15. NUMBER OF PAGES
Fault detection; Turbine wheels; Cracks; TF-41 engine	53
	16. PRICE CODE

17. SECURITY CLASSIFICATION OF REPORT	18. SECURITY CLASSIFICATION OF THIS PAGE	19. SECURITY CLASSIFICATION OF ABSTRACT	20. LIMITATION OF ABSTRACT
Unclassified	Unclassified	Unclassified	